The Thesis Committee for Yiwei Ma
Certifies that this is the approved version of the following thesis:

Diagnosis of Induced Hydraulic Fractures during Polymer Injection

APPROVED BY
SUPERVISING COMMITTEE:

Supervisor:

Mark W. McClure

Matthew Balhoff

Diagnosis of Induced Hydraulic Fractures during Polymer Injection

by

Yiwei Ma, B.E., M.S.

Thesis

Presented to the Faculty of the Graduate School of

The University of Texas at Austin

in Partial Fulfillment

of the Requirements

for the Degree of

Master of Science in Engineering

The University of Texas at Austin
May 2015

Dedication

To my family, advisors, co-workers and friends

Acknowledgements

First and foremost, I'd like to thank my advisor Dr. Mark M. McClure for the offer of pursuing my Master's degree under his supervision. Mark has been a great advisor, for generously sharing his knowledge and experience, inspiring me with enthusiasm and encouragement. Joining without any previous background in petroleum engineering or computational modeling, I felt difficult to start and follow the study and research at the beginning. Mark gave me a lot of support and guidance through responsive feedbacks and numerous discussions.

I'd also love to sincerely acknowledge Dr. Gary Pope for granting me the opportunity of joining CEOR JIP and sponsoring my study. I really appreciated Dr. Pope's guidance with so many invaluable insights and suggestions on my research. It was a great honor for me to learn from him, not only his outstanding expertise, but also his considerate and humble attitude.

Special thanks to Dr. Mojdeh Delshad for providing parameters of the viscoelastic model that I applied to my research. Thank Zhitao Li, a Ph.D. student working with Dr. Delshad, for all the suggestions and discussions.

Last but not the least, I want to extend my gratitude to my dear family for their tireless support, and to all my lovely friends for making the two year journey at UT enjoyable and unforgettable.

Abstract

Diagnosis of Induced Hydraulic Fractures during Polymer Injection

Yiwei Ma, M.S. E.

The University of Texas at Austin, 2015

Supervisor: Mark W. McClure

Polymer transport with complex fluid rheology was implemented into an existing hydraulic fracturing simulator (CFRAC), and the implementation was extensively validated. Shear thinning viscosity was included for polymer fluid flow in both porous media and fractures. Shear thickening viscosity was implemented for flow in the matrix.

Polymer injections were simulated to investigate the effect of polymer rheology, including both shear thinning and shear thickening behaviors, on polymer injectivity and on the possibility of induced hydraulic fracturing. The results indicated that shear thickening decreases injectivity and can induce initiation of hydraulic fractures. The hydraulic fractures substantially enhance injectivity, and eliminate the reduction in injectivity due to shear thickening.

Pressure fall off tests were simulated to study the effect of polymer rheology on the identification of hydraulic fractures from the shut-in transient after shut-in. The results showed that standard methods from pressure transient analysis can be applied to diagnose the presence hydraulic fracturing by identifying a linear flow regime and fracture closure on a Bourdet derivative plot and a square root of time plot. It was found that these methods are effective regardless of shear thickening and shear thinning rheology. However, the results suggested that if the fracture is small and closes quickly, this could cause difficulty for the diagnosis.

Table of Contents

List of Tables

List of Figures

Chapter 1: Research Objectives and Chapter Descriptions

1.1 RESEARCH OBJECTIVES

Polymer flooding is applied as a tertiary oil recovery process after water flooding in heavy oil reservoirs. Polymer flooding can provide better mobility control and enhanced reservoir sweep efficiency, but the viscous nature of the polymer solution can substantially decrease the well injectivity (Sheng et al., 2015). However, unexpectedly high injectivity has been observed in many field applications and induced hydraulic fracturing has been proposed as a potential cause (Wang et al., 2008; Lee, 2012; Moe Soe Let et al., 2012). Therefore, diagnosis of induced hydraulic fracturing is essential for differentiation from other possible mechanisms that could cause high injectivity and for evaluating its effect on the polymer flooding process. Because more than 90% of field applications use partially hydrolyzed polyacrylamide (HPAM), HPAM rheology is taken as representative for polymer injection modeling in this particular study.

The objectives of this study were:

- to implement polymer transport and HPAM rheology functions into an existing hydraulic fracturing simulator (CFRAC) in order to model polymer fluid flow in porous media and fractures
- to investigate the effect of polymer rheology on polymer injectivity and hydraulic fracture initiation
- to simulate pressure fall-off (PFO) tests and perform pressure transient analysis in order to investigate diagnostic strategies for hydraulic fracturing during polymer injection

1.2 CHAPTER DESCRIPTIONS

In Chapter 2, polymer flooding is introduced in terms of the process, polymer types and properties, rheology models, injectivity, and pressure transient analysis. Near the end of Chapter 2, injectivity associated with induced hydraulic fractures and pressure transients of fractured wells are discussed.

In Chapter 3, the simulator applied in this study, Complex Fracturing ReseArch Code (CFRAC), is described. The modeling details are described, including systems of equations for polymer mass balance, two polymer rheology models for fluid flow in porous media and fractures, and the numerical methods used to solve the system of equations. In Chapter 4, model validation is provided using simulation results.

In Chapter 5, eight simulation cases are described. The simulations can be categorized into two groups, depending on the difference between the minimum principal stress and the initial reservoir pressure. In each group of simulation cases, all the settings are identical except: (1) polymer rheology and (2) whether a hydraulic fracture is permitted to form during the simulation. For polymer rheology, two different settings are applied. For flow in the matrix, the simulations either consider only shear shinning, or include both shear thinning and thickening. The simulation results are discussed, in terms of the effects of polymer rheology and induced hydraulic fractures on injectivity and on the pressure transients after shut-in. The shut-in pressure transient results are analyzed to determine whether the presence of hydraulic fractures can be diagnosed.

Chapter 6 summarizes the main conclusions of the study.

Chapter 2: Introduction and Literature Review

2.1 POLYMER FLOODING PROCESS

Polymer flooding, a chemical enhanced oil recovery (EOR) technique, has gained great popularity in recent decades because it increases sweep efficiency and improves fractional flow characteristics (Standnes and Skjevrak, 2014). High-viscosity polymer fluid can improve mobility ratio, reduce viscous fingering, and enhance areal sweep efficiency (Pye and Gogarthy, 1964; Sandiford, 1964). In reservoirs containing significant heterogeneities in the vertical direction, viscous polymer fluid helps to divert the injected water into bypassed or poorly swept zones (Needham and Doe, 1987). In addition to the viscosity effect, some polymers can reduce the relative permeability of the water phase more than the relative permeability of the oil phase. Therefore, polymer flooding can increase the fractional flow of oil, which increases oil recovery (Sheng et al., 2015).

Polymer flooding can be applied independently, or combined with other chemical injections, including surfactant-polymer flooding and alkaline-surfactant-polymer flooding. Successful field applications have been reported, especially in Daqing and Chateaurenard (Wang et al., 2008; Takaqi et al., 1992). By 2004, about 23% of the total production at the Daqing field was estimated to be due to polymer injection, representing an incremental production of 10% of the original oil in place (Wang et al., 2008). In the Courtenay area of the Chateaurenard field, 31% of the original oil in place was recovered after 17 years of production, half of which originated from the polymer injection (Putz et al., 1988). With improved economics and a track record of success, polymer flooding has become the most commonly applied chemical EOR technique.

2.2 POLYMER TYPES AND PROPERTIES

There are two general types of EOR polymers, synthetic polymers and biopolymers. Partially hydrolyzed polyacrylamide (HPAM) is the most commonly used synthetic polymer, while Xanthan gum is a typical biopolymer. In general, higher polymer concentration and larger molecular weight yield higher viscosity.

Many studies have compared these two polymers in terms of rheology, salinity sensitivity, thermal stability, degradation resistance, cost, and other parameters.

For fluid flow in porous media at low velocities, both HPAM and Xanthan have been reported to show shear thinning behavior (Cannella et al., 1988; Seright et al., 2009), in which fluid viscosity decreases with increased velocity and shear rate. At moderate-to-high velocities, Xanthan continues to show shear thinning behavior (Cannella et al., 1988; Seright et al., 2009). However, the viscosity of HPAM starts to increase with increased velocity and shear rate, an effect called shear thickening (Smith, 1970; Masuda et al., 1992; Hirasaki and Pope, 1972). The shear thickening property of HPAM is a result of the "viscoelastic behavior." The rheology of HPAM solutions is described in more detail in Section 2.3. It has also been observed in laboratory coreflood experiments that the viscoelasticity of HPAM can help to lower the residual oil saturation (Wang et al., 2001; Huh and Pope, 2008).

Concerning the effect of salinity, HPAM is much more salt sensitive than Xanthan, because the negative carboxyl group in the HPAM molecule interacts with cations, which reduces the viscosity of the polymer solution substantially (Sheng, 2010; Chang, 1978). As a result, HPAM is usually preferred in low salinity conditions, while Xanthan is better for viscosity maintenance in high salinity waters (Needham and Doe, 1987).

It is common to encounter high temperature in reservoir conditions. Therefore, the thermal stability of the polymer is important for maintaining the designed viscosity. At high temperature, the polymer molecule may experience hydrolysis and lose effectiveness. It has been reported that HPAM can keep good thermal stability until 110°C, but Xanthan is only suitable for temperatures less than 80°C (Sheng, 2010).

There are three main kinds of degradation that can affect polymer performance. Chemical degradation can be caused contaminants such as oxygen and ferric ions. Additives like thiourea, have been tested as a way to reduce chemical degradation (Ayirala et al., 2010). Biodegradation can occur for either Xanthan or HPAM, but is more likely with Xanthan. Mechanical degradation is the breakdown of polymer molecule due to high shear stress at high flow velocity. This is usually encountered during the polymer preparation process and near the wellbore. Previous studies have found that Xanthan is more resistant to mechanical shearing effects (Seright et al., 2009).

Although HPAM and Xanthan both have advantages and disadvantages, HPAM is more widely applied in field applications due to lower cost, better biodegradation resistance, and relative permeability reduction (Lake, 2010). A recent literature review investigated 72 field applications of polymer flooding and reported 92% of the projects used HPAM (Standnes and Skjevrak, 2014).

This thesis is primarily focused on investigating the rheology and reservoir behavior of HPAM.

2.3 HPAM RHEOLOGY

2.3.1 HPAM molecular structure

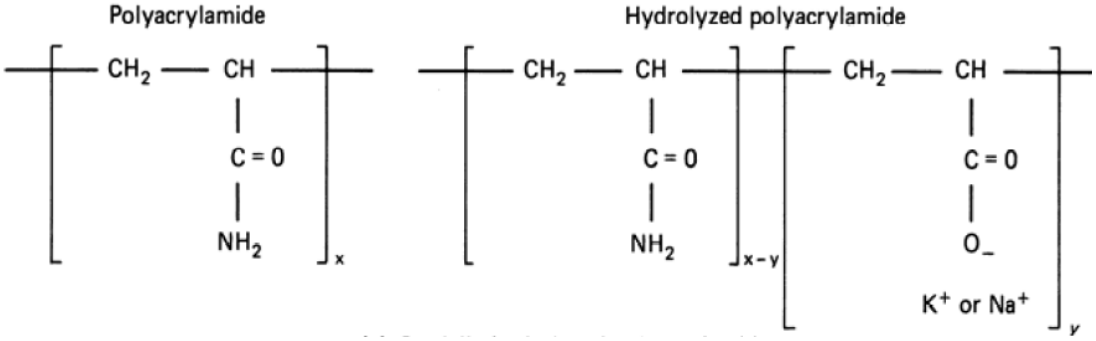

Figure 2-1 molecular structure of partially hydrolyzed polyacrylamide (HPAM)

HPAM is a large-weight molecule with monomeric units of acrylamide forming a flexible chain structure (Figure 2-1). Part of the polyacrylamides are hydrolyzed, leaving negatively charged carboxyl groups (—COO^-) scattered along the chain. The repulsive forces between these anions, either within the same molecule or between different molecules, allow HPAM molecules to elongate and contract, resulting in high viscosity (Lake, 2010). This mechanism also explains why HPAM is sensitive to salinity and hardness. Cations react with the carboxyl groups and reduce the viscosity.

The shear thickening behavior of HPAM can also be explained based on its molecular structure. Unlike Xanthan gum, which has a more branched and rigid molecular structure, the chain structure of HPAM makes it flexible. In porous media, HPAM elongates and contracts while flowing through pore bodies and pore throats. At high flow velocities, HPAM molecules do not have sufficient relaxation time to stretch, re-coil, and adjust to the flow (Delshad et al., 2008). As a result, the apparent viscosity becomes very high, observed as shear thickening behavior.

2.3.2 Apparent shear rate

For non-Newtonian fluids such as HPAM and Xanthan gumn, viscosity is a function of shear rate. The shear rate of fluid can be easily controlled in a viscometer. However, there is not a simple link between these measurements and the apparent shear rate in porous media. Coreflood experiments can be conducted, but they are very time consuming. Additionally, each core represents a unique reservoir condition. Cannella et al. (1988) proposed an equation for apparent shear rate (Eqn. 2-1) using the capillary bundle model:

$$\gamma_{eff} = C\left[\frac{3n+1}{4n}\right]^{n/(n-1)}\left[\frac{u_w}{\sqrt{kk_{rw}S_w\phi}}\right], \qquad \text{Eqn. 2-1}$$

where, u_w is Darcy velocity of the fluid, k is the permeability of the porous media, k_{rw} is the relative permeability of water phase, S_w is water saturation, and ϕ is porosity. Cannella et al. (1988) reported that C = 6 can match a wide variety of coreflood data. Wreath et al. (1990) developed other expressions for apparent shear rate.

2.3.3 Shear thinning model

Shear thinning is characterized by a decrease in viscosity with increased shear rate. Away from the wellbore, the displacement process of polymer flooding is relatively slow, and HPAM solution shows shear thinning behavior.

A simple but popular shear thinning model is the power law model (Eqn. 2-2) (Bird et al., 1960):

$$\eta = m\dot{\gamma}^{n-1}, \qquad \text{Eqn. 2-2}$$

where, $\dot{\gamma}$ is shear rate, η is apparent viscosity, and *m*, *n* are constants characterizing the fluid. This simple relation is used by many simulators because it describes the non-Newtonian viscosity curve over the linear portion of the log-log plot of viscosity versus shear rate.

Another curve that can be used to fit most lab data is the Carreau equation (Carreau, 1972):

$$\frac{\eta-\eta_\infty}{\eta_0-\eta_\infty}=\left[1+\left(\lambda\dot{\gamma}\right)^2\right]^{(n-1)/2}, \qquad \text{Eqn. 2-3}$$

where, η_0 is the zero shear rate viscosity, η_∞ is the infinite shear rate viscosity, λ is a parameter with units of time, *n* is a dimensionless parameter. Although the power law model is simple and easy to implement, the Carreau equation avoids having an unrealistic infinite viscosity at zero shear rate.

2.3.4 Viscoelastic (shear thickening) model

The opposite of shear thinning, shear thickening is defined as an increase in fluid viscosity with increased shear rate. Injection fluid usually experiences high flow velocity and shear rate near the wellbore. HPAM solution shows shear thickening at moderate-to-high shear rate. Therefore, use of a solely shear thinning model will cause underestimation of the viscosity of HPAM solution near the wellbore.

The Deborah number (N_{Deb}) is a ratio of the relaxation time for a polymer molecule to the characteristic period for elongation and contraction as the fluid flows through the porous media (Bird et al., 1977). It is used to characterize a polymer's elastic

strain and is applied in shear thickening models (Hirasaki and Pope, 1972; Masuda et al., 1992; Delshad et al., 2008). By relating the Deborah number and apparent shear rate, Delshad *et al.* (2008) proposed the following shear thickening model:

$$\mu_{el} = \mu_{\max}\left[1-\exp\left(-\left(\lambda_2 \tau_r \dot{\gamma}_{eff}\right)^{n_2-1}\right)\right], \qquad \text{Eqn. 2-4}$$

where, μ_{el} is shear thickening viscosity, $\mu_{\max}$, λ_2, and n_2 are empirical constants, τ_r is the relaxation time for a polymer molecule.

2.3.5 Unified viscosity model

To characterize the viscosity of HPAM solution over a wide range of Darcy velocity and shear rate, Delshad et al. (2008) combined the shear thickening model with the Carreau equation and proposed a unified viscosity model for HPAM solution. This unified viscosity model has the advantage of needing only bulk rheology data and petrophysical information about the porous media:

$$\mu_{app} = \mu_w + (\mu_p^0 - \mu_w)\left[1+\left(\lambda\dot{\gamma}_{eff}\right)^2\right]^{(n-1)/2} + \mu_{\max}\left[1-\exp\left(-\left(\lambda_2\tau_r\dot{\gamma}_{eff}\right)^{n_2-1}\right)\right], \qquad \text{Eqn. 2-5}$$

where, μ_{app} is apparent polymer viscosity, μ_w is water viscosity, n, n_2 and λ_2 are empirical constants. μ_p^0 is the zero shear rate viscosity modeled as a function of the polymer concentration and effective salinity. λ, $\mu_{\max}$ and τ_r are functions of the polymer concentration. $\dot{\gamma}_{eff}$ is evaluated using Cannella equation (Eqn. 2-1).

2.4 POLYMER INJECTIVITY

Polymer injectivity is a key parameter for field applications but is hard to predict. Dominant mechanisms governing polymer injectivity include polymer rheology, debris in the polymer solution, mechanical degradation, and fracturing (Yerramilli et al., 2013; Seright et al., 2009).

2.4.1 HPAM rheology

In Section 2.3, the rheology of HPAM solution was described in detail. Although HPAM solutions exhibit shear thinning in a viscometer, investigators consistently report shear thickening behavior in porous rock at high shear rate (Pye and Gogarthy, 1964; Smith, 1970; Seright, 1983; Hirasaki and Pope, 1972). When HPAM solution is injected into a reservoir, high flux near the wellbore should be expected to yield high fluid viscosity due to the shear thickening effect, reducing the injectivity.

2.4.2 Debris in the polymer

During the preparation of polymer solution, ineffectively hydrated polymer and other debris may remain in the polymer fluid, especially when the solution is unfiltered. This may lead to plugging of the sand face at the wellbore, reducing the polymer injectivity (Treiber and Yang, 1986).

2.4.3 Mechanical degradation

In opposition to the effects of shear thickening and debris plugging, polymer injectivity could be increased by mechanical degradation. HPAM can be susceptible to mechanical degradation (Seright, 1983). Breakdown of polymer molecules could lead to loss of fluid viscosity, an increase in injectivity, and decreased mobility control. Mechanical degradation can happen at the surface when the polymer injection fluid goes through irregular paths in high pressure drop equipment such as chokes and valves

(Standnes and Skjevrak, 2014). This can be minimized by mixing the solution carefully and removing chokes during the preparations (Greaves et al., 1984). Mechanical degradation can occur in the formation near the wellbore and in the perforations due to the high flow velocity and shearing effect. Away from the wellbore, flow velocity decreases and no further significant mechanical degradation should take place (Seright, 1983).

2.4.4 Induced fractures

According to Van den Hoek *et al*. (2008), most water injectors operate under induced fracturing conditions. Considering the viscous nature of polymer solution, injection above the formation parting pressure is even more likely during polymer flooding (Seright et al., 2009). Induced fracturing has been proposed as an explanation for the high polymer injectivity observed in many field applications (Wang et al., 2008; Seright et al., 2009; Lee, 2012; Moe Soe Let et al., 2012; Denney, 2013).

Under proper circumstances, induced fractures could increase oil productivity and sweep efficiency (Wang et al., 2008; Lee, 2012; Crawford and Collins, 1954; Dyes et al., 1958). In one example of a successful application, a well was fractured intentionally to maintain the polymer injectivity. An increased production rate and decreased water cut was observed along with the propagation of the fracture (Fletcher et al., 2013). On the other hand, induced fractures may reduce sweep efficiency if they have unfavorable orientation or divert fluids into only certain layers of a layered reservoirs (Lee, 2012).

2.5 PRESSURE TRANSIENT ANALYSIS

Pressure fall-off (PFO) testing is a common technique that provides important information about well performance, formation parameters, and in-situ mobility. PFO testing consists of analyzing pressure transient signal produced after shut-in of an

injection well. Van den Hoek *et al*. (2012) developed an interpretation method for PFO tests during polymer injection to characterize in-situ polymer rheology and induced fracture dimensions. This study assumed polymer solution only exhibited shear thinning behavior. However, shear thickening behavior of HPAM solution is nonnegligible in porous media, especially near the wellbore where fractures could be induced (Hirasaki and Pope, 1972; Seright, 1983; Smith, 1970). An objective of this study is to do numerical modeling of PFO testing with both shear thinning and thickening effects.

Fractured wells may encounter three flow regimes, namely linear flow, bilinear flow and radial flow (Figure 2-2).

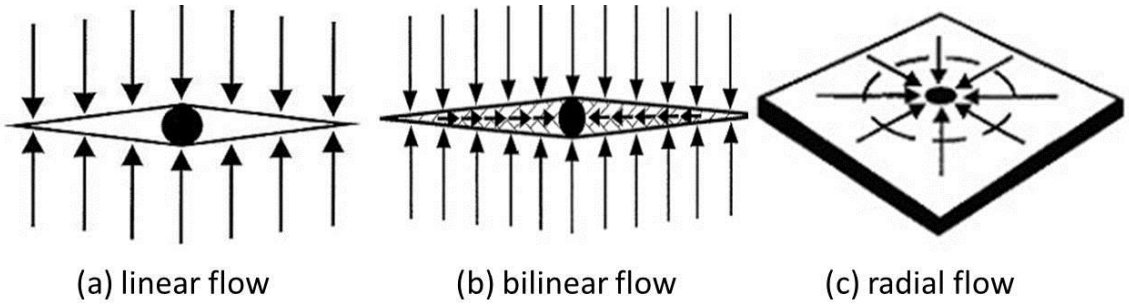

Figure 2-2 flow regimes for fractured wells

The relationship between fracture conductivity and reservoir conductivity is key for differentiating the three flow regimes. It is characterized by a dimensionless term, C_{fD}, which is defined as:

$$C_{fD} = \frac{k_f w}{k L_f}, \qquad \text{Eqn. 2-6}$$

where, w is the average aperture of the fracture, and k_f is the permeability of the fracture defined as:

$$k_f = \frac{w^2}{12}. \qquad \text{Eqn. 2-7}$$

If C_{fD} is greater than 300, the fracture has effective infinite conductivity and the well will show linear flow at early time. If C_{fD} is smaller than 300 but greater than 0.1, the fracture is finite conductivity, and the well may show both bilinear and linear flow. If C_{fD} is smaller than 0.1, the fracture has negligible conductivity and has no effect on the pressure transient.

Both linear and bilinear flow regimes are good indications of the presence of hydraulic fractures connecting to the well. There are some diagnostic curves based on the flow behaviors to visualize and determine the flow regimes. The basic flow equations are first introduced below and the diagnostic plots are explained later.

- **linear flow**

  In linear flow, the pressure drop can be written in a function:

$$\Delta P = \frac{4.06qB}{hL_f}\sqrt{\frac{\mu t}{k\phi c_t}}, \qquad \text{Eqn. 2-8}$$

where ΔP is the difference between the bottom hole pressure and the pressure at the beginning of the transient, q is the injection rate in volume per time, B is the formation factor, h is fracture height, μ is viscosity, c_t is compressibility factor. This equation shows that ΔP is proportional to $\sqrt{t}$. Eqn. 2-8 can also be written in the log form as:

$$\log(\Delta P) = \frac{1}{2}\log(t) + \log(\frac{4.06qB}{hL_f}\sqrt{\frac{\mu}{k\phi c_t}}), \qquad \text{Eqn. 2-9}$$

Eqn. 2-10 and Eqn. 2-11 can be derived by taking the derivative of ΔP with respect to t. As implied by Eqn. 2-9, Eqn. 2-10, and Eqn. 2-11, both ΔP and $\frac{\partial(\Delta P)}{\partial t}\cdot t$ are proportional to $\sqrt{t}$. A $\frac{1}{2}$ slope becomes a diagnostic signal for linear flow in both the pressure plot ($\Delta P \sim t$) and the derivative plot ($\frac{\partial(\Delta P)}{\partial t}\cdot t \sim t$) in log-log scales.

$$\frac{\partial(\Delta P)}{\partial t}\cdot t = \frac{2.03qB}{hL_f}\sqrt{\frac{\mu t}{k\phi c_t}}. \qquad \text{Eqn. 2-10}$$

$$\log(\frac{\partial(\Delta P)}{\partial t}\cdot t) = \frac{1}{2}\log(t) + \log(\frac{2.03qB}{hL_f}\sqrt{\frac{\mu}{k\phi c_t}}). \qquad \text{Eqn. 2-11}$$

- **bilinear flow**

  In bilinear flow, the flow equation is:

$$\Delta P = \frac{44.1qB\mu}{h\sqrt{k_f w}\left(\phi\mu c_t k\right)^{1/4}}\sqrt[4]{t}, \qquad \text{Eqn. 2-12}$$

  Similarly, the derivative form of bilinear flow equation is:

$$\frac{\partial(\Delta P)}{\partial t}\cdot t = \frac{11.025qB\mu}{h\sqrt{k_f w}\left(\phi\mu c_t k\right)^{1/4}}\sqrt[4]{t}. \qquad \text{Eqn. 2-13}$$

Therefore, both ΔP and $\frac{\partial(\Delta P)}{\partial t}\cdot t$ are proportional to $\sqrt[4]{t}$. A $\frac{1}{4}$ slope becomes a diagnostic signal for bilinear flow in both the pressure plot ($\Delta P \sim t$) and the derivative plot ($\frac{\partial(\Delta P)}{\partial t}\cdot t \sim t$) in log-log scales.

- **radial flow**

  The flow equation for radial flow is:

$$\Delta P = \frac{q\mu}{4\pi kh}\ln(\frac{4kt}{1.78\phi\mu c_t r_w^2}), \qquad \text{Eqn. 2-14}$$

where r_w is the wellbore radius. The log form and the derivative form of the equation are written as:

$$\Delta P = \frac{2.31q\mu}{4\pi kh}\log(\frac{4kt}{1.78\phi\mu c_t r_w^2}). \qquad \text{Eqn. 2-15}$$

$$\frac{\partial(\Delta P)}{\partial t}\cdot t = \frac{q\mu}{4\pi kh}. \qquad \text{Eqn. 2-16}$$

Chapter 3: Methodology

3.1 COMPLEX FRACTURING RESEARCH CODE (CFRAC)

Complex Fracturing ReseArch Code (CFRAC) was developed by Dr. Mark McClure and Dr. Roland Horne between 2010 and 2012 at Stanford University. From the beginning of 2013, development has been ongoing in Dr. McClure's research group at The University of Texas at Austin. The simulator is written in C++ and visualization is performed in MATLAB. The full details of CFRAC are summarized in Chapter 2 of McClure (2012).

CFRAC simulates fluid flow in discrete fracture networks (DFN), with leak-off from the fracture into the surrounding matrix. Flow in the matrix can be simulated fully numerically with an unstructured mesh. The model calculates the stresses induced by opening and sliding along individual fractures and couples opening and slip to fracture transmissivity. A new 3D version of CFRAC is available, but for the simulations in this research, the 2D version was used. CFRAC can be run in plane strain or with the psuedo-3D adjustment of Olson (2004). In CFRAC, the systems of equations are coupled using iterative coupling. The structure of the code is illustrated in Figure 3.1. The main advantage of iterative coupling is that it allows separate modules for each problem. Compared to solving the entire system of equations all at once, iterative coupling can be less computationally expensive.

CFRAC assumes an isothermal, isotropic, and homogeneous reservoir and single-phase flow. For this study, the ability to simulate polymer transport and complex fluid rheology was implemented into CFRAC. Polymer transport is simulated with a system of mass balance equations in a separate module. Polymer rheology functions were

implemented into the system of flow equations, updating the fluid viscosity and the flow calculations.

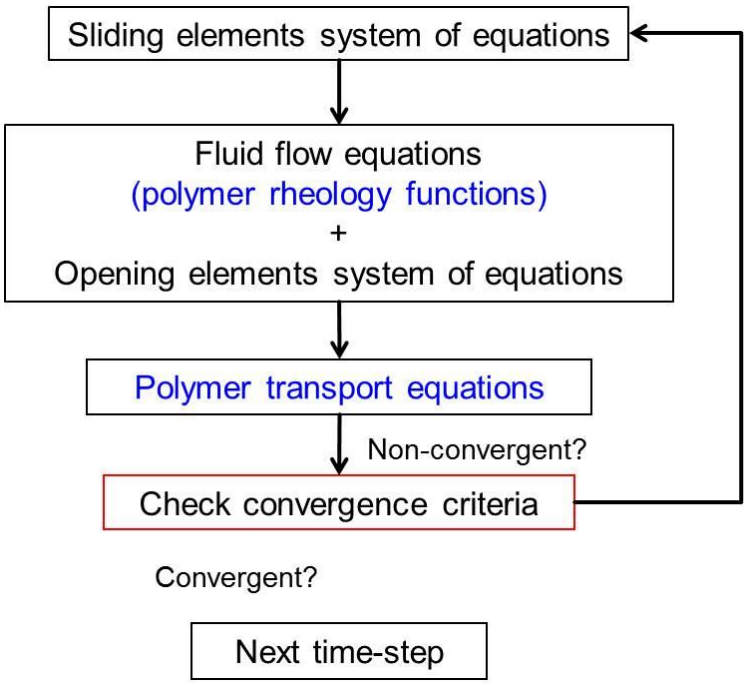

Figure 3-1 summary of the iterative coupling approach for a single time step. The steps labeled in blue were newly implemented for this study.

3.2 POLYMER MASS BALANCE EQUATIONS

The finite volume method is used to simulate polymer transport. As it is shown in Figure 3-1, the system of polymer transport equations is solved in a separate module, with pressure, stresses, and flow rates calculated in other modules. Polymer dispersion and adsorption are neglected, and the simulations are single-phase and isothermal. The unsteady state polymer mass balance equation for a fracture element is:

$$\frac{\partial(EC_p)}{\partial t} + \nabla \cdot (u_{flux} e C_p) = 0, \qquad \text{Eqn. 3-1}$$

where C_p is the polymer concentration for a single fracture element (mass per volume), E is the void aperture (the fluid storage per area), t is time, e is the hydraulic aperture (the thickness of aperture available for flow) and u_{flux} is the fluid flux (volumetric flow rate per cross-sectional area). The fluid flux is calculated in a separate model and held constant in the polymer transport module.

The unsteady state polymer mass balance equation for a matrix element is:

$$\frac{\partial(\phi C_p)}{\partial t} + \nabla \cdot (u_{flux} C_p) = 0, \qquad \text{Eqn. 3-2}$$

where ϕ is the porosity of the matrix.

3.2.1 Explicit method

In the explicit method, polymer concentrations in the system are calculated using values from the previous time step. The discrete mass balance equations are:

$$\frac{(V_{frac} C_p)_i^{n+1} - (V_{frac} C_p)_i^n}{\Delta t} + \sum_k (q_{ik}^n C_{p,ik}^n) = 0, \qquad \text{Eqn. 3-3}$$

$$\frac{(V_{pore} C_p)_i^{n+1} - (V_{pore} C_p)_i^n}{\Delta t} + \sum_k (q_{ik}^n C_{p,ik}^n) = 0, \qquad \text{Eqn. 3-4}$$

where V_{frac} and V_{pore} are the volume of the fracture element and the pore volume of matrix element, respectively, i is the index of the element, n is time step, t is time, q_{ik} is

the flow rate between element *i* and element *k* with a negative sign if the fluid is flowing out of element *i*. In the flow terms, C_p is up-winded using the polymer concentration of the element with higher pressure.

In the explicit method, the polymer concentration (C_p) of the flow terms is calculated using the value for the previous time step (n).

3.2.2 Implicit method

In the implicit method, polymer concentrations in the system at the next time step are calculated from the values in the current time step. This creates a system of equations. The system of equations is linear because the mass flow rates are assumed constant. The residual functions of the fracture and matrix elements are:

$$R(C_{p,i}^{n+1}) = \frac{(V_{frac}C_p)_i^{n+1} - (V_{frac}C_p)_i^n}{\Delta t} + \sum_k (q_{ik}^{n+1} C_{p,ik}^{n+1}), \qquad \text{Eqn. 3-5}$$

$$R(C_{p,i}^{n+1}) = \frac{(V_{pore}C_p)_i^{n+1} - (V_{pore}C_p)_i^n}{\Delta t} + \sum_k (q_{ik}^{n+1} C_{p,ik}^{n+1}), \qquad \text{Eqn. 3-6}$$

where, $R(C_{p,i}^{n+1})$ is the polymer residual function (a function of the polymer concentration) of the element *i* at $(n+1)^{th}$ time step and element *i* can either be a fracture element or a matrix element in the two equations above. Δt is the time stepping between n^{th} and $(n+1)^{th}$ time step. Unlike the explicit method, the implicit method evaluates the flow terms at $(n+1)^{th}$ time step. The vector of the unknowns consists of the polymer concentrations of all the elements in the simulation (C_p^{n+1}). At time step $(n+1)$, the initial guess for C_p^{n+1} is C_p^n, the solution vector from last time step.

The explicit method is easier to implement. However, it is numerically unstable unless very small time steps are taken. As a result, the implicit method is much more efficient.

3.3 HPAM RHEOLOGY MODELS

There has been relatively little investigation of polymer fluid rheology during flow in fractures. A previous study did coreflood experiments using cores with smooth and rough fractures and found that the HPAM solution was only shear thinning when flowing through the fractures, never shear thickening (Zechner et al., 2013). This is apparently because fracture apertures are sufficiently large that significant contraction-expansion of the polymer molecule does not occur.

Based on these arguments from the literature, different rheology functions were used for polymer fluid flow in porous media and fractures. Both shear thinning and shear thickening viscosities were included for polymer fluid flow in porous media. Only shear thinning viscosity was used for flow in fractures. The models and related parameters are explained in the following two sections.

3.3.1 HPAM rheology function in porous media

The unified model (Eqn. 2-5) was proposed to calculate the polymer viscosity in porous media (Delshad et al., 2008). The values of the associated parameters are explained in the following section and summarized in Table 3-1. More details can be found in Section 20 in UTCHEM manual (Delshad et al., 2000). In Eqn. 2-5, μ_p^0 is the zero shear rate viscosity, defined as a function of the polymer concentration and solution salinity (Eqn. 3-10).

$$\mu_p^0 = \mu_w \left[1 + \left(A_{p1} C_p + A_{p2} C_p{}^2 + A_{p3} C_p{}^3 \right) C_{SEP}^{S_p} \right], \qquad \text{Eqn. 3-10}$$

where $C_{SEP}^{S_p}$ is the effective salinity in meq/ml, A_{p1}, A_{p2} and A_{p3} are model parameters obtained from laboratory data. Since CFRAC doesn't keep track of salinity, a set of lab experimental data with S_p equal to zero was selected to eliminate the effect of salinity.

$$\lambda = \beta_1 \exp(\beta_2 C_p), \qquad \text{Eqn. 3-11}$$

$$\mu_{\max} = \mu_w \left(AP_{11} + AP_{22} \ln C_p \right), \qquad \text{Eqn. 3-12}$$

$$\tau_r = \tau_0 + \tau_1 C_p, \qquad \text{Eqn. 3-13}$$

where, β_1, β_2, AP_{11}, AP_{22}, τ_0, and τ_1 are model parameters obtained from laboratory measurements.

The apparent shear rate, $\dot{\gamma}_{eff}$, is evaluated using Cannella equation (Eqn. 2-1). Because CFRAC only has single-phase fluid flow, both k_{rw} and S_w are equal to 1. Thus, the equation for the apparent shear rate can be re-written as:

$$\dot{\gamma}_{eff} = C \left[\frac{3n+1}{4n} \right]^{n/(n-1)} \left[\frac{u_w}{\sqrt{k\phi}} \right], \qquad \text{Eqn. 3-14}$$

In CFRAC, the polymer viscosity functions are implemented within the system of fluid flow equations by updating the flow terms in the residual functions and derivative terms in the Jacobian matrix.

For each flow term in the fluid flow residual functions, the flow between elements (mass flow rate per time) is calculated as a function of pressure. For polymer fluid flow, the viscosity has to be updated using the rheology functions discussed above in order to

calculate the flow terms. First, the Darcy velocity, u_w, is calculated using an initial guess of apparent viscosity. Then the apparent shear rate ($\dot{\gamma}_{eff}$) and the polymer viscosity are calculated using Eqn. 3-14 and Eqn. 2-5, respectively. Iterations are performed with the secant method until the difference between the guess value and updated value of the apparent viscosity is within a reasonable tolerance level.

For each derivative term in the Jacobian matrix, the derivative of the residual function with respect to pressure is calculated. After implementation of the polymer rheology function, the fluid viscosity becomes a function of pressure, and this needs to be included in the derivatives in the Jacobian. The derivative of the fluid viscosity with respect to pressure is numerically evaluated as:

$$\frac{\partial \mu_{app}}{\partial P} \approx \frac{\mu_{app}(P+\Delta P) - \mu_{app}(P)}{\Delta P}, \qquad \text{Eqn. 3-15}$$

where ΔP is a small change in pressure. The apparent viscosity is re-evaluated with pressure of $P+\Delta P$ to obtain another new value of apparent viscosity $\mu_{app}(P+\Delta P)$ using the same iteration process described above. If the change in viscosity is too small, numerical roundoff error can cause the approximation to be inaccurate. To avoid this, the code performs a check after the difference is calculated, and if necessary, the procedure is repeated with a larger value of ΔP.

parameters	values	parameters	values
μ_w	0.001 Pa·s	λ_2	0.01
n	0.78	n_2	3.5
A_{p1}	35	AP_{11}	21.764
A_{p2}	435	AP_{22}	3.4964
A_{p3}	1055	τ_0	0.008905
β_1	0.0192	τ_1	0.2992
β_2	18.522	C	6

Table 3-1 parameters for unified rheology model of HPAM solution

3.3.2 HPAM rheology function in fractures

The unified rheology model (Eqn. 2-5) consists of a shear thinning and shear thickening part. The first part is based on the Carreau equation (Eqn. 2-3) for modeling shear thinning viscosity. It is now applied for polymer fluid flow in fractures and re-written as:

$$\mu_{app} = \mu_w + (\mu_p^0 - \mu_w)\left[1+\left(\lambda\dot{\gamma}_{eff}\right)^2\right]^{(n-1)/2}, \qquad \text{Eqn. 3-16}$$

where all the parameters are consistent with the ones applied in Eqn. 2-5, and the values can be found in Table 3-1.

The polymer fluid flow in the fracture is modeled as linear flow in a slit (Figure 3-2). With no analytical solution of the apparent shear rate available in current literature, the apparent viscosity for fracture flow must be calculated numerically.

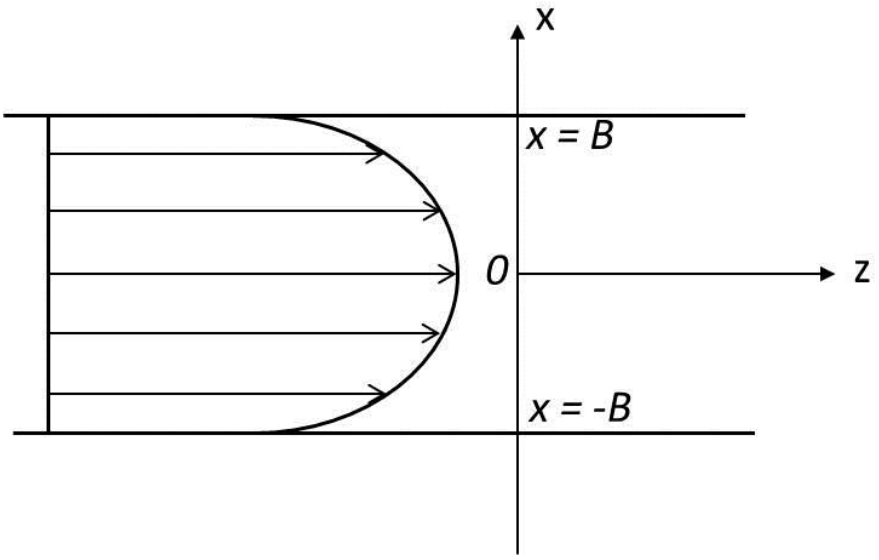

Figure 3-2 polymer fluid flow in the fracture

First, the flow velocity profile along the aperture of the fracture is calculated numerically by coupling the rheology function and momentum balance equation (Eqn. 3-17 ~ Eqn. 3-19).

$$\tau_i = \{\mu_w + (\mu_p^0 - \mu_w)\left[1+\left(\lambda\dot{\gamma}_{eff,i}\right)^2\right]^{(n-1)/2}\} * \dot{\gamma}_{eff,i}, \quad \text{Eqn. 3-17}$$

$$\tau_i = \frac{\Delta P}{L} x_i, \quad \text{Eqn. 3-18}$$

$$\dot{\gamma}_{eff,i} = \frac{v_{i+1} - v_{i-1}}{2\Delta x}, \quad \text{Eqn. 3-19}$$

The flow velocities are discretized to multiple elements across the aperture. In the three equations above, τ_i is the shear stress at element *i*, $\dot{\gamma}_{eff,i}$ is the shear rate at element

i (which is calculated from velocities of neighbored elements using the finite difference method), x_i is the coordinate of element i based on the coordinate system shown in Figure 3-2, ΔP is the pressure drop between two elements, L is the distance between two elements, which is the average length of the two fracture elements, and Δx is the distance between two neighbored elements along the aperture.

Residual functions are defined based on Eqn. 3-17 ~ Eqn. 3-19 as:

$$R_i = \left\{ \mu_w + (\mu_p^0 - \mu_w) \left[1 + \left(\lambda \cdot \frac{v_{i+1} - v_{i-1}}{2\Delta x} \right)^2 \right]^{(n-1)/2} \right\} * \frac{v_{i+1} - v_{i-1}}{2\Delta x} - \frac{\Delta P}{L} x_i , \qquad \text{Eqn. 3-20}$$

The system of equations is solved using the Newton-Raphson method. Because the problem is 1D, the Jacobian matrix is bidiagonal, and can be solved very efficiently. An average value of viscosity is calculated based on the distribution of fluid velocity and viscosity along the fracture aperture.

In the fluid flow module, the derivative of viscosity with respect to pressure is numerically evaluated using Eqn. 3-15, similar to the method used for matrix flow.

Chapter 4: Model Validations

4.1 VALIDATION OF CFRAC WITH KGD MODEL

The Khristianovich-Geertsma-de Klerk (KGD) model is a two-dimensional (2D) model for hydraulic fracture propagation. The assumption of the fracture geometry is shown in Figure 4-1. In the KGD model, the fracture height is assumed constant and the fluid is assumed to be a Newtonian fluid with constant viscosity. The relationship between aperture and pressure is calculated with a plane strain assumption, with the plane cut along the fracture length. This means that the fracture stiffness scales with fracture length, unlike the PKN model where fracture stiffness scales with fracture height. Assuming zero leakoff, the equations for fracture half length (x_f) and the maximum fracture width (w_0) at the center of the fracture are (Valkó and Economides, 1995):

$$x_f = 0.428\left[\frac{q^3 G}{(1-\nu)\mu h^3}\right]^{1/6} t^{2/3} \qquad \text{Eqn. 4-1}$$

$$w_0 = 1.487\left[\frac{(1-\nu)q^3\mu}{Gh^3}\right]^{1/6} t^{1/3} \qquad \text{Eqn. 4-2}$$

where x_f is the half-length of the fracture in m, w_0 is the maximum width of the fracture in m, q is injection rate in m^3/s, μ is fluid viscosity in Pa·s, h is fracture height in m, G is shear modulus in Pa, ν is the Poisson ratio, and t is time in s.

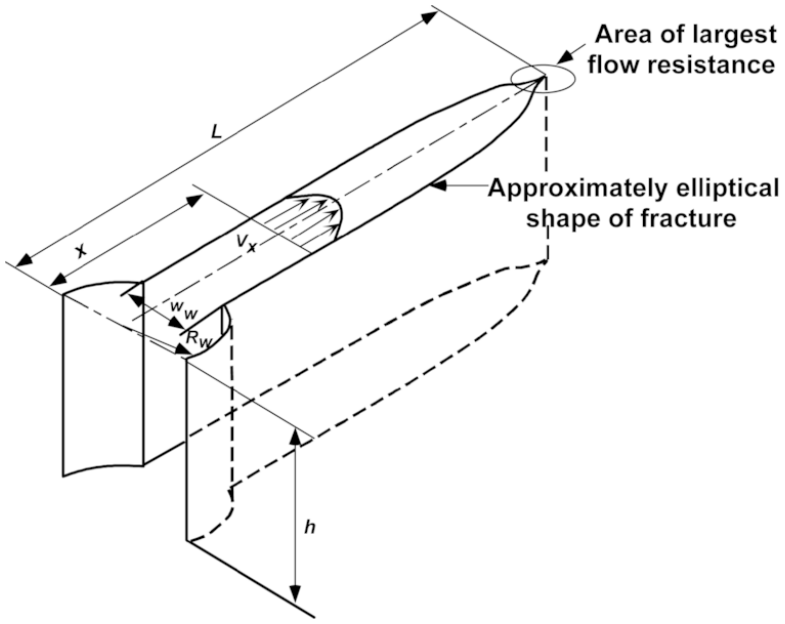

Figure 4-1 fracture geometry in KGD model

For validation, a simulation was run in CFRAC to simulate the propagation of a single hydraulic fracture. A CFRAC simulation of a single fracture in plane strain is analogous to the KGD model. The results for the fracture dimensions (the half-length and maximum width of the fracture) were compared to the analytical solutions from the KGD model. The settings of the simulation are summarized in Table 4-1 and the simulation results are demonstrated in Figure 4-2 and Figure 4-3. The simulation results were consistent with KGD analytical solutions. The match for fracture width at the well was nearly perfect. The match was not quite as good for the comparison based on fracture length, but still very close. The difference was probably because of assumptions in the KGD model related to the pressure distribution very close to the crack tip.

Parameter	Values
injection rate, q	0.1 m^3/s
reservoir height, h	100 m
water viscosity, μ	0.001 Pa·s
shear modulus, G	1.5×10^{10} Pa
Poisson ratio, ν	0.25

Table 4-1 simulation settings for CFRAC validation with KGD model

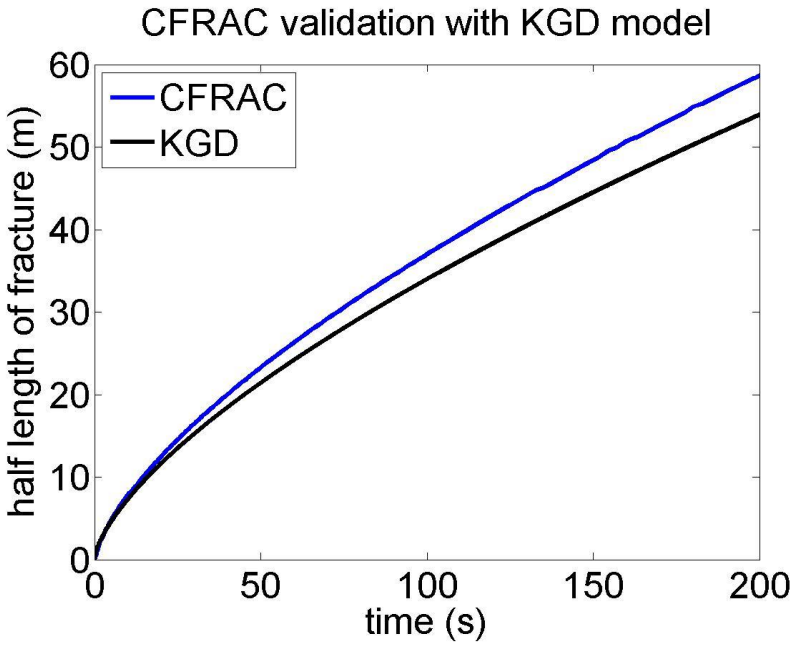

Figure 4-2 the fracture half-length from the simulation result and KGD solution

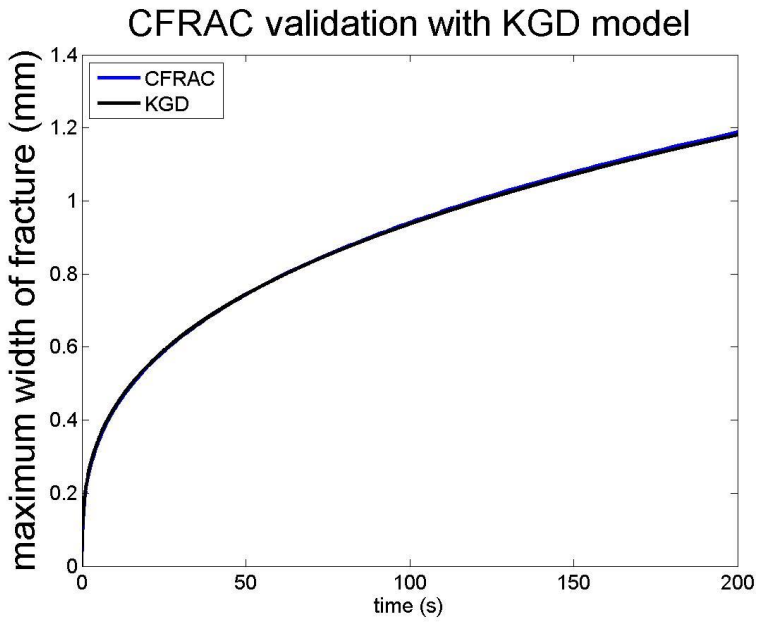

Figure 4-3 the fracture maximum width from the simulation result and KGD solution

4.2 VALIDATION OF POLYMER TRANSPORT IN CFRAC

If the polymer rheology functions are not used (described in Section 3.3), the polymer behaves simply like a solute. A validation for the polymer transport was conducted by simulating 1D advective flow. In the simulation, water was injected for a sufficiently long time to reach steady state, forming a constant pressure gradient from wellbore to the two edges of the problem domain. Then, polymer at a specified concentration was introduced to the injection fluid, while the injection rate was maintained constant. The main settings in the simulation are summarized in Table 4-2. Figure 4-4 shows the polymer transport front during the simulation.

Parameter	Values
injection concentration, $C_{p,inj}$	2000 ppm
injection rate, q	0.1 m^3/s
porosity, ϕ	20%
permeability, k	300 mD
reservoir height, h	100 m

Table 4-2 simulation settings for polymer transport validation

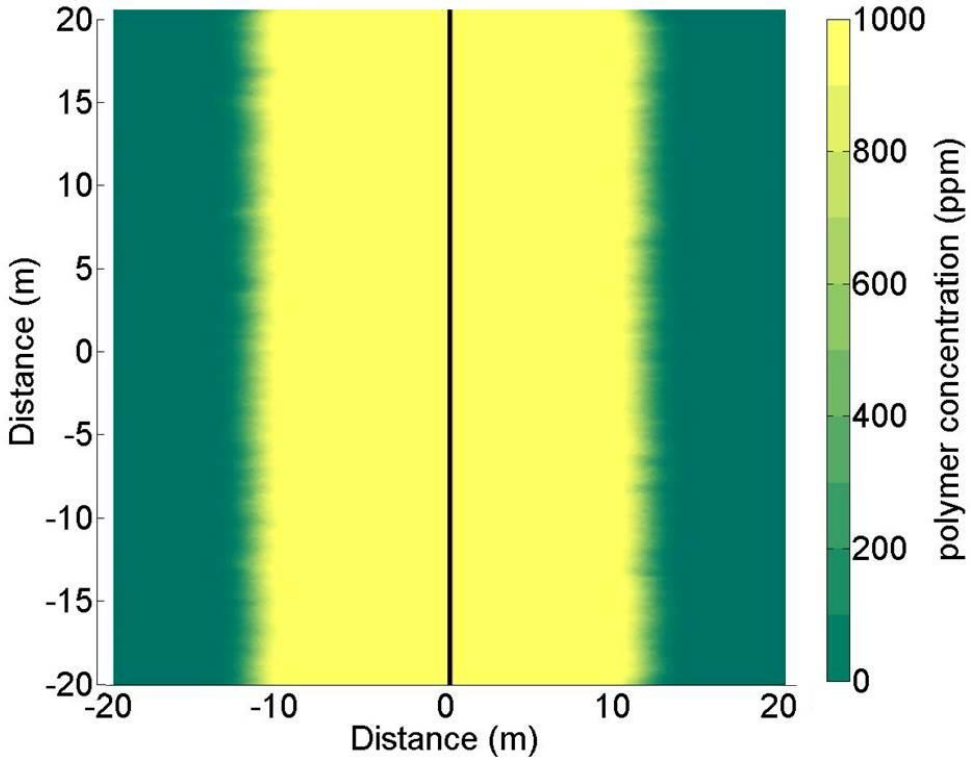

Figure 4-4 visualization of polymer transport front of 1D advective flow

In Figure 4-4, the black vertical line is the wellbore and constant pressure boundaries are set at the left and right edges of the domain. The upper and lower edges are no-flow boundaries. The sharp front of the polymer transport is consistent with expected result of 1D advective flow.

To better understand numerical dispersion, simulations with different element sizes were conducted and the results were compared. Figure 4-5 shows the polymer transport front by plotting the polymer concentration versus distance away from the wellbore. Three different simulation cases are shown, each with a different element size. Different line styles in the figure represent results at three different times during the simulations. The results indicate that the numerical dispersion cannot practically be eliminated in the simulation but can be effectively reduced by using sufficiently small elements.

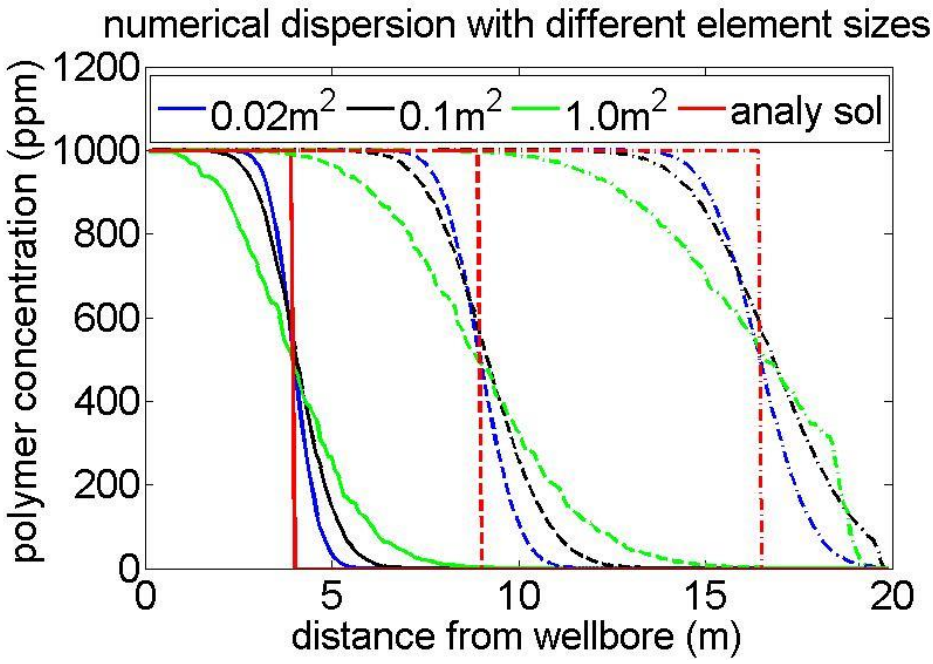

Figure 4-5 numerical dispersion in polymer transport with different element sizes

4.3 VALIDATION OF HPAM RHEOLOGY MODEL IN POROUS MEDIA

Based on the unified model in Eqn. 2-5, HPAM rheology curves with different polymer concentrations are shown in Figure 4-6. For all three curves, as shear rate moves from high to low, the viscosity decreases due to the shear thickening effect and then increases due to the shear thinning effect. For radial flow in porous media with a constant injection rate, the flow velocity decreases away from the wellbore, and accordingly, the shear rate decreases as well. With shear thickening and shear thinning, the viscosity should be high at the wellbore, decrease with distance, and then increase again. Based on this hypothesis, a simulation of radial flow of polymer solution was set up. The simulation settings are summarized in Table 4-3.

The viscosity distribution was visualized to validate the implementation of both shear thinning and shear thickening viscosity functions (Figure 4-7). Figure 4-7 shows that the viscosity was very high near the wellbore. Away from the wellbore, viscosity decreased due to the transition from shear thickening to shear thinning. At further distance, viscosity increased again due to the diminishing shear thinning effect. This is consistent with the rheology curves in Figure 4-6 and also our expectation for the behavior of the system.

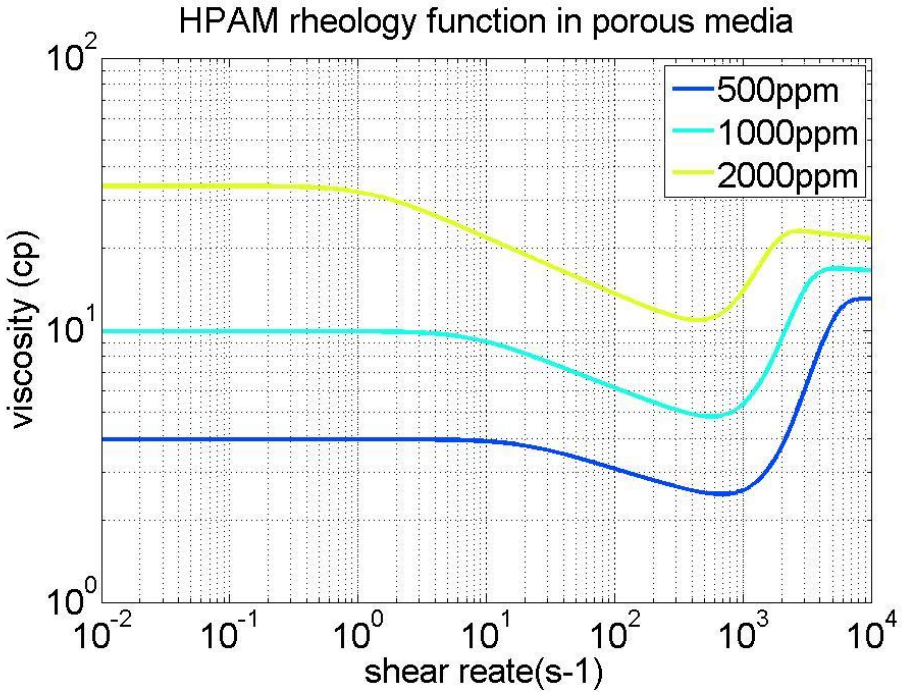

Figure 4-6 HPAM rheology in porous media at different concentrations

Parameter	Values
injection concentration, $C_{p,inj}$	1000 ppm
injection rate, q	0.05 m^3/s
porosity, ϕ	10%
permeability, k	500 mD
reservoir height, h	100 m

Table 4-3 simulation settings for HPAM rheology validation

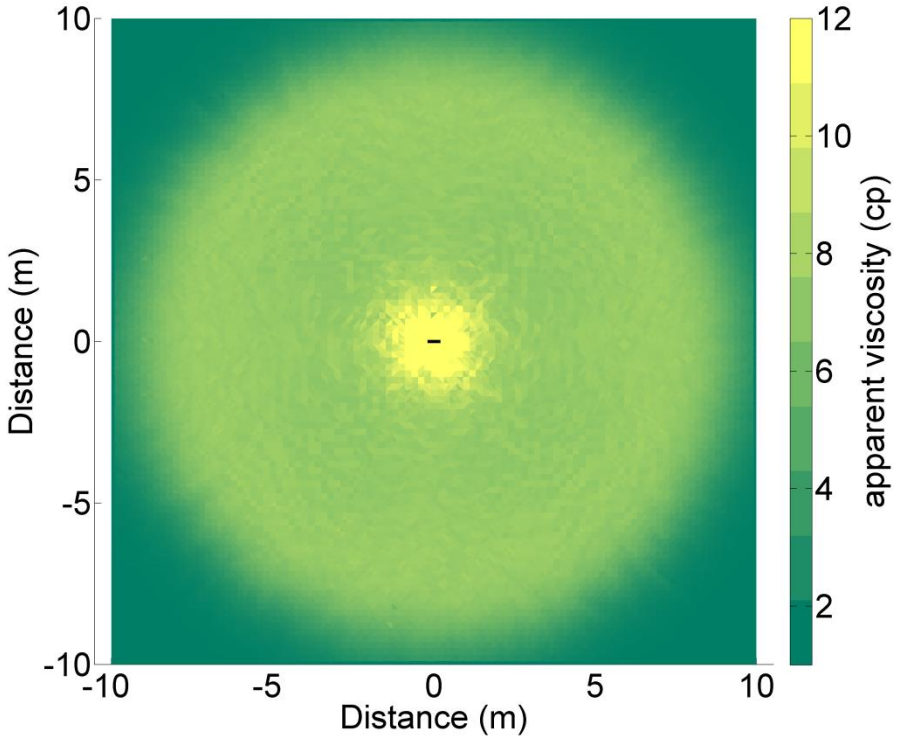

Figure 4-7 viscosity distribution of polymer radial flow

4.4 VALIDATION OF PRESSURE TRANSIENT RESULTS FROM CFRAC

For validation, radial flow of water (without polymer) was simulated, and the pressure transient results were analyzed. Water injection was simulated until steady state and then the well was shut-in to monitor the pressure transient. The simulation settings are summarized in Table 4-4. The pressure data was interpreted based on Eqn. 2-14 ~ Eqn. 2-16. The results are shown in Figure 4-8 and Figure 4-9.

Parameter	Values
injection rate, q	0.004 m^3/s
water viscosity, μ	0.001 Pa·s
porosity, ϕ	20%
permeability, k	300 mD
reservoir height, h	20 m

Table 4-4 simulation settings for pressure transient results validation

Based on Eqn. 2-14 and the settings in Table 4-4, the expected semilog derivative of pressure can be calculated as:

$$\frac{\partial(\Delta P)}{\partial \ln(t)} = \frac{q\mu}{4\pi kh} = \frac{0.004 m^3/s \times 0.001 Pa \cdot s}{4\pi \times (300 \times 10^{-15} m^2) \times 20 m} = 53,052 Pa .$$

This analytical derivative value was compared to the values from the simulation results. From Figure 4-8 and 4-9, the derivative terms during the injection and after the shut-in are:

$$\frac{\partial(\Delta P)}{\partial \ln(t)} = 7.50 psi = 51,711 Pa , \qquad \frac{\partial(\Delta P)}{\partial \ln(t)} = 7.40 psi = 51,021 Pa .$$

Both values are comparable to the analytical solution.

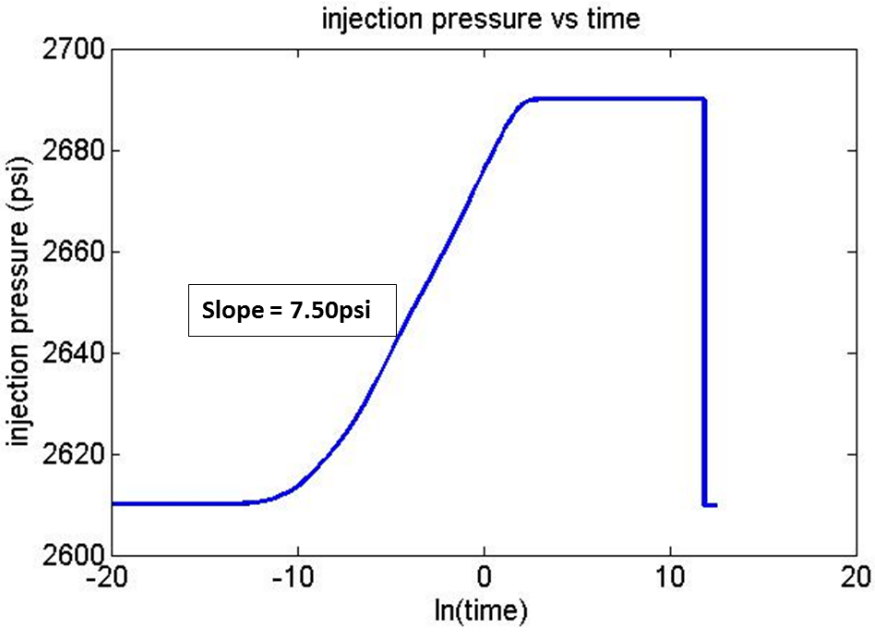

Figure 4-8 pressure transient during water injection (no frac)

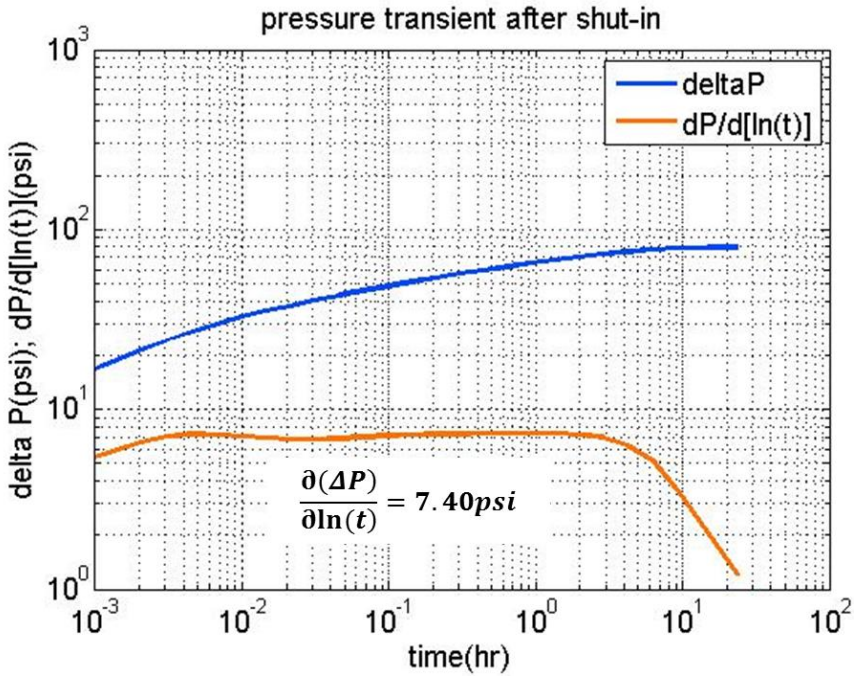

Figure 4-9 pressure transient after well shut-in (water injection, no frac)

Chapter 5: Results and Discussions

5.1 SIMULATIONS OF POLYMER INJECTIONS

Polymer injections were simulated with settings summarized in Table 5-1. The well was set in the middle of the problem domain and injected polymer solution at a constant rate and specified polymer concentration. Constant pressure boundaries were set at all four edges of the problem domain so that steady state would be reached at late time. Once steady state was established, the well was shut-in for pressure transient monitoring.

The eight simulations were divided into two groups with different remote stresses. In one group, the remote stresses were much higher than the pore pressure in the reservoir. In the other group, the remote stresses were close to the pore pressure in the reservoir, representing an overpressured formation.

Within each group of simulation, four cases were simulated, varying two variables: the presence of an induced hydraulic fracture and the polymer rheology. In some simulations, it was assumed as a model assumption that a hydraulic fracture could not form. In the simulations where the hydraulic fracture was permitted to form, it was assumed to be a single linear feature. For the polymer rheology, it was assumed that either there was only shear thinning in the matrix or that there was a combination of both shear thinning and shear thickening in the matrix. As discussed in Section 3.3, shear thinning only was always assumed for flow in the fractures. The four simulations were combinations of with/without the induced hydraulic fracture and with/without shear thickening in the matrix.

Parameters	Group 1	Group 2
maximum horizontal stress, S_{Hmax}	3770 psi	2900 psi
minimum horizontal stress, S_{hmin}	3770 psi	2900 psi
initial reservoir pressure, P_{pore}	2610 psi	2610 psi
reservoir area, A	200 m × 200 m	200 m × 200 m
reservoir height, h	20 m	20 m
permeability, k	300 mD	300 mD
porosity, %	20	20
injection rate, q	0.004 m^3/s	0.004 m^3/s
injection polymer concentration, $C_{p,inj}$	1000 ppm	2000 ppm

Table 5-1 simulation settings for polymer injection cases

5.2 POLYMER INJECTIVITY ANALYSIS

5.2.1 Polymer injection without induced hydraulic fractures

Figure 5-1 and Figure 5-2 show the polymer injectivity for the regular pore pressure and overpressured cases, respectively. In both cases, shear thickening decreased the polymer injectivity by causing extra pressure drop near the wellbore, where the shear rate was high. This result is consistent with previous studies on the HPAM rheology in porous media (Seright, 1983; Hirasaki and Pope, 1972).

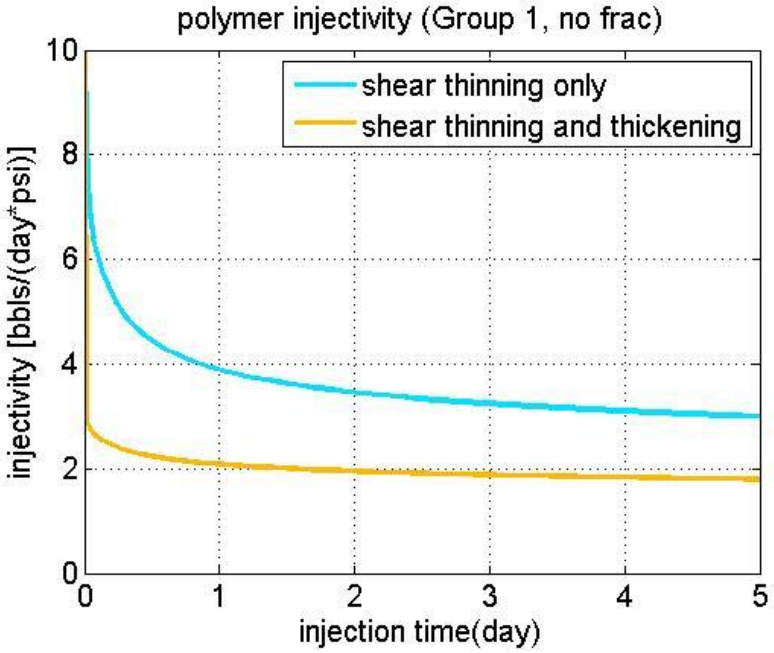

Figure 5-1 the polymer injectivity for the normal pore pressure cases (Group 1, no frac)

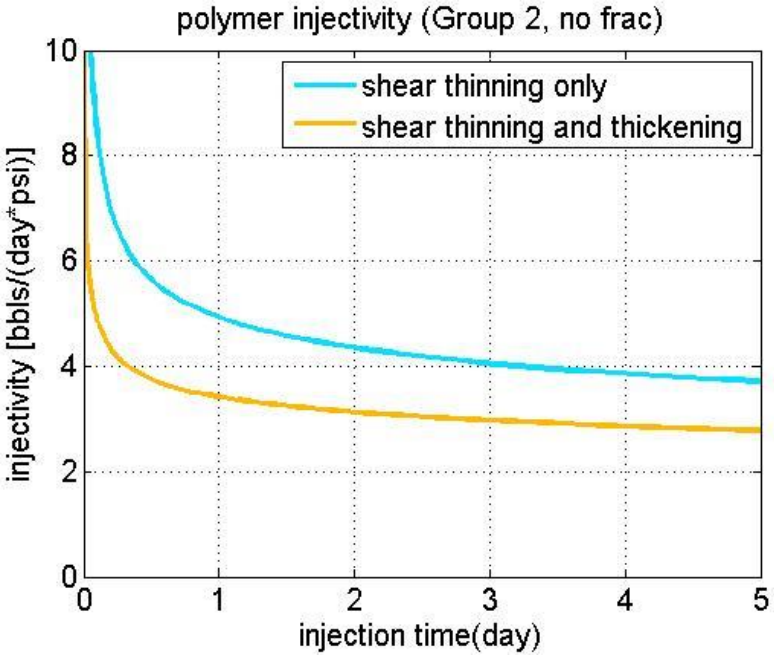

Figure 5-2 the polymer injectivity for the overpressured cases (Group 2, no frac)

5.2.2 Polymer injection with induced hydraulic fractures

Figure 5-3 and Figure 5-4 show the polymer injectivity for simulation cases with an induced hydraulic fracture. The presence of the fracture increased the polymer injectivity by a factor of 1.7 ~ 4.0 compared to the simulations with no fracture. The polymer injectivity in the two simulations with and without shear thickening stabilized at the same injectivity level. The large pressure drop caused by the shear thickening effect was relieved by the high conductivity of the fracture. By allowing fluid to leak out into the matrix over a larger area, the fracture prevented the very high Darcy velocity at the wellbore and reduced the overall amount of shear thickening.

The fracture half-length was only 10m in the regular pressure reservoir, but as long as 150m in the overpressured reservoir. The fracture length was different in these two cases because leakoff from the fracture was more rapid in the simulations where the minimum principal stress (and therefore fracture opening pressure) was much greater than the reservoir pressure.

Fracture initiations can be identified in Figure 5-3 and Figure 5-4 from the abrupt increase in the polymer injectivity. Fracture initiation occurred much earlier in the cases with shear thickening. In the normal reservoir pressure simulations, the fractures were induced at about 17.5 hrs and 75.5 days for the cases with and without shear thickening effect, respectively. In the overpressured reservoir simulations, the initiation times were about 95 s and 6.5 hrs for the cases with and without shear thickening, respectively.

To verify the fracture initiation times mentioned above, movies were made of fracture aperture as a function of time. The movies confirmed that initiation occurred at the point identified from the injectivity plots. The pressure transients during the injections (Figure 5-5 ~ Figure 5-8) also indicated fracture initiation at these times.

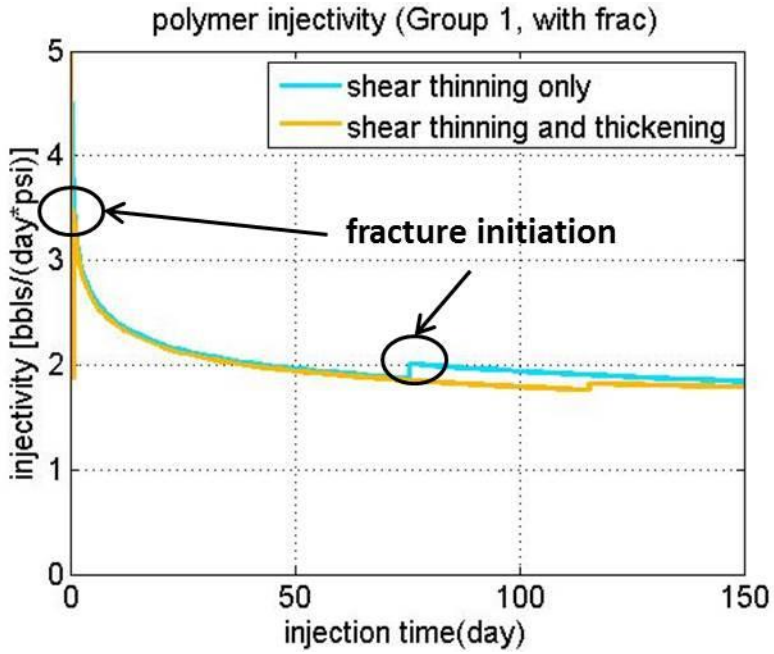

Figure 5-3 polymer injectivity for the normal pore pressure cases (Group 1, with frac)

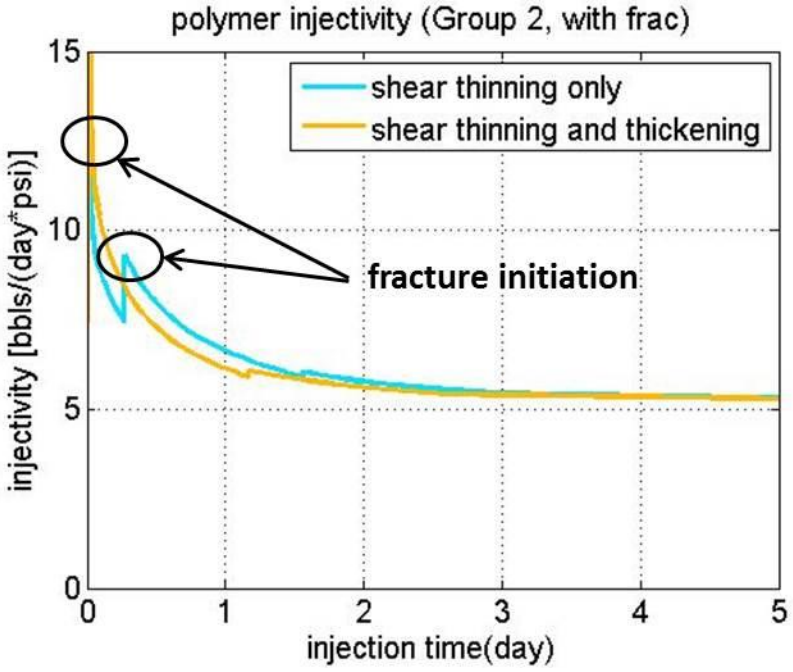

Figure 5-4 polymer injectivity for the overpressured cases (Group 2, with frac)

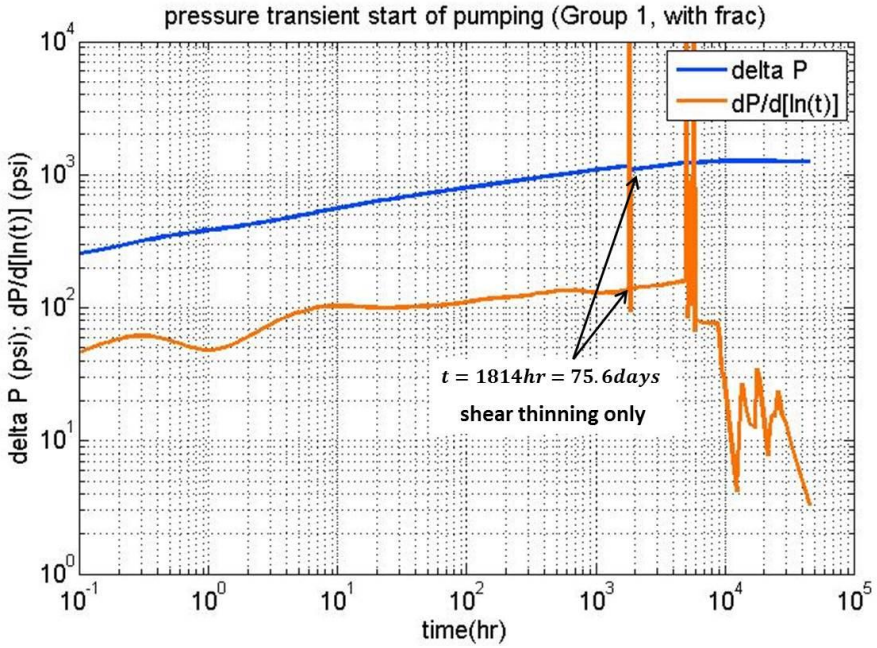

Figure 5-5 pressure transient of the polymer injection in normal pore pressure cases (Group 1, with frac, shear thinning only)

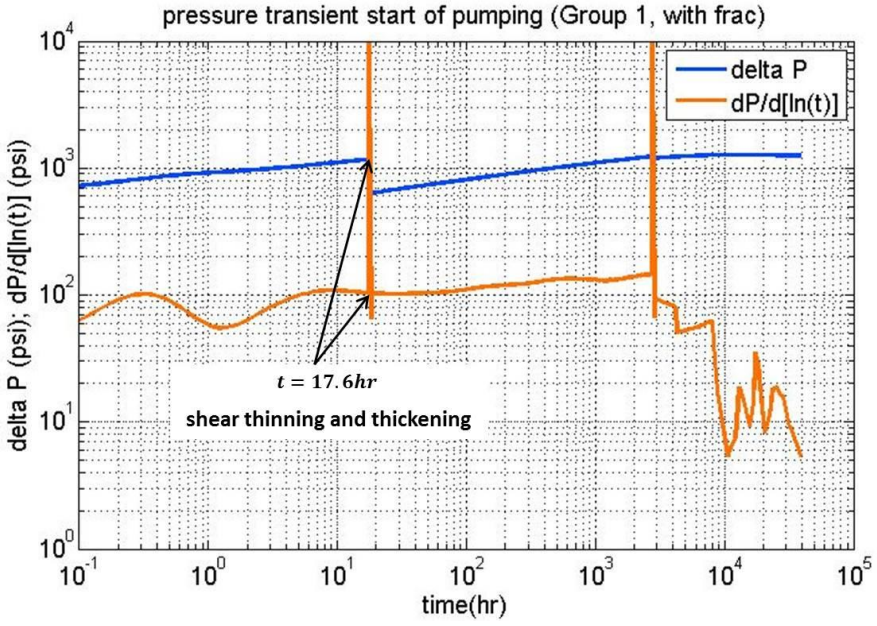

Figure 5-6 pressure transient of the polymer injection in normal pore pressure cases (Group 1, with frac, with shear thickening)

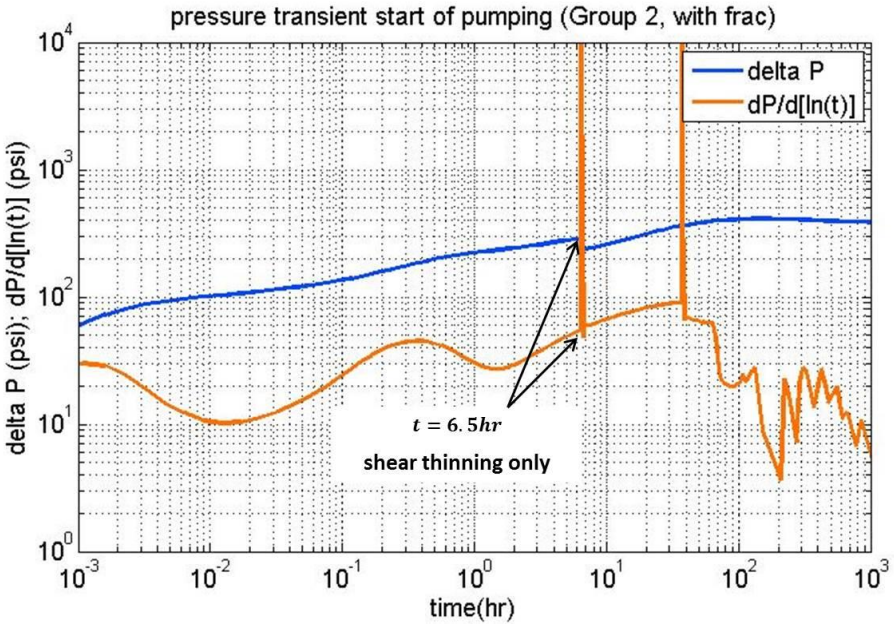

Figure 5-7 pressure transient of the polymer injection in normal pore pressure cases (Group 2, with frac, shear thinning only)

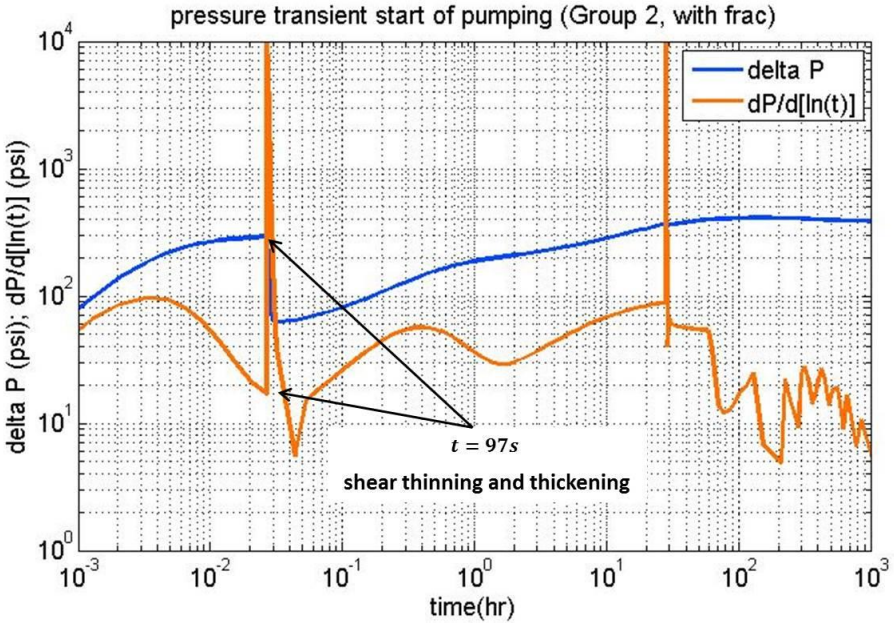

Figure 5-8 pressure transient of the polymer injection in normal pore pressure cases (Group 2, with frac, with shear thickening)

To investigate the initiation process and better visualize the viscosity distributions with and without the shear thickening effect, two additional simulations were conducted with a very small element size of 0.1 m and a small domain of 20 m × 20 m. All other settings were identical to those in the group 2 in Table 5-1. Figure 5-9 shows the viscosity distributions near the wellbore right before the fracture initiations, at 1.67 hrs and 3.5min, for the cases without and with shear thickening cases, respectively. With the shear thickening effect, the viscosity near the wellbore was much higher than the case without shear thickening effect, explaining the earlier fracture initiation.

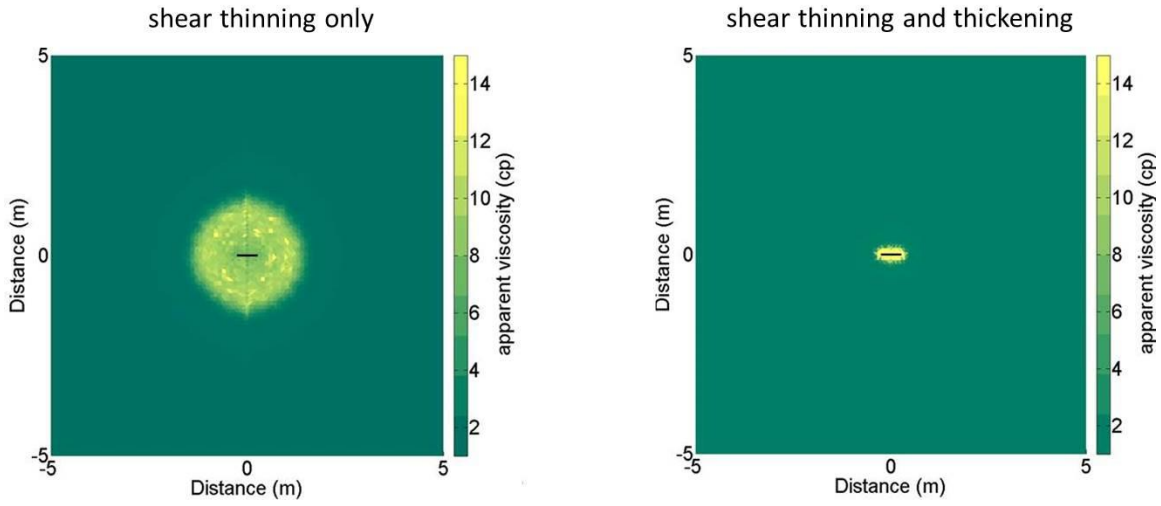

Figure 5-9 viscosity distributions near the wellbore with/without shear thickening effect at the moment before fracture initiations.

To summarize, the shear thickening effect decreased the polymer injectivity and encouraged earlier initiation of the hydraulic fracture due to the high viscosity near the wellbore. However, the hydraulic fracture effectively eliminated the detrimental

injectivity of the shear thickening. After the hydraulic fracture formed, the injectivity of the shear thinning and the shear thickening/thinning simulations were nearly identical.

5.3 PRESSURE TRANSIENT ANALYSIS

In our simulations, the pressure transients after shut-in were easier to interpret than the pressure transients during the initial polymer injection. During the initial injection, the polymer transport front was propagating away from the well. Spatial differences in polymer concentration within the reservoir affect the fluid viscosity, and therefore affect the pressure transients. To avoid these complications, we focused our analysis on the shut-in transients. Polymer injection was simulated for a sufficiently long time to achieve steady state prior to shut-in. Therefore, the polymer concentration was uniform in the whole problem domain, and signals from the pressure transients were either due to the polymer rheology or due to the presence of induced hydraulic fractures.

5.3.1 Well shut-in without induced hydraulic fractures

In this group of simulations, hydraulic fractures were not permitted to form, as a model assumption. Three kinds of fluids with different rheology functions were tested: a Newtonian fluid with constant viscosity, polymer fluid with shear thinning viscosity in the matrix only, and polymer fluid with both shear thinning and thickening viscosity in the matrix. As described in Section 3.3, the fluid was assumed only shear thinning in the fractures, except in the case where it was assumed to be a Newtonian fluid.

Figure 5-10 ~ Figure 5-13 show the pressure transient results in the derivative plots for the normal fluid pressure and overpressured cases, respectively. In all cases, the derivative curve plunges to zero at later time, which is a typical effect for a shut-in test and is also caused by the constant pressure boundaries at the problem edge.

Prior to the plunge, the derivative curve shows the pressure transient behavior due to radial flow in the reservoir. For the Newtonian fluid, the curve is flat, as expected. Based on Eqn. 2-16, for radial flow, the derivative term, $\frac{\partial(\Delta P)}{\partial t} \cdot t$, is proportional to μ, with all other variables constant in the simulations.

The simulations with non-Newtonian fluids had different trends in the derivative plots. After shut-in, the flow velocity began to slow down everywhere in the reservoir. Lower velocity yields lower shear rate, which affects the fluid viscosity accordingly. For both reservoir pressure conditions, the derivative curves increased over time, indicating an increasing fluid viscosity, and thus shear thinning behavior (since shear rate was decreasing). The domination of the shear thinning effect is also indicated by the identical plots for the cases with and without the shear thickening effect. At early time after shut-in, the derivative term for the shear thickening case showed a sharp decrease, representing a decline in the viscosity and thus the shear thickening behavior.

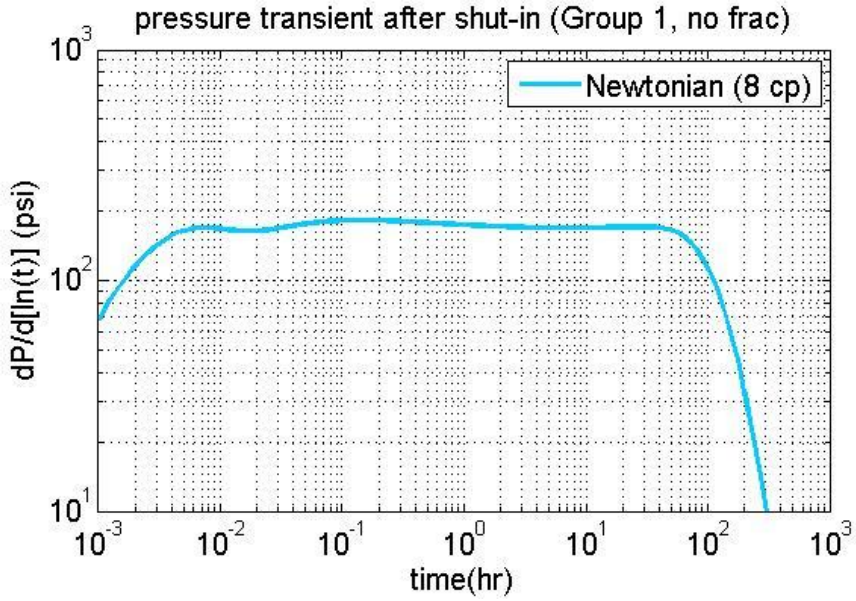

Figure 5-10 shut-in pressure transients of the Newtonian fluid for the regular pore pressure cases (Group 1, no frac)

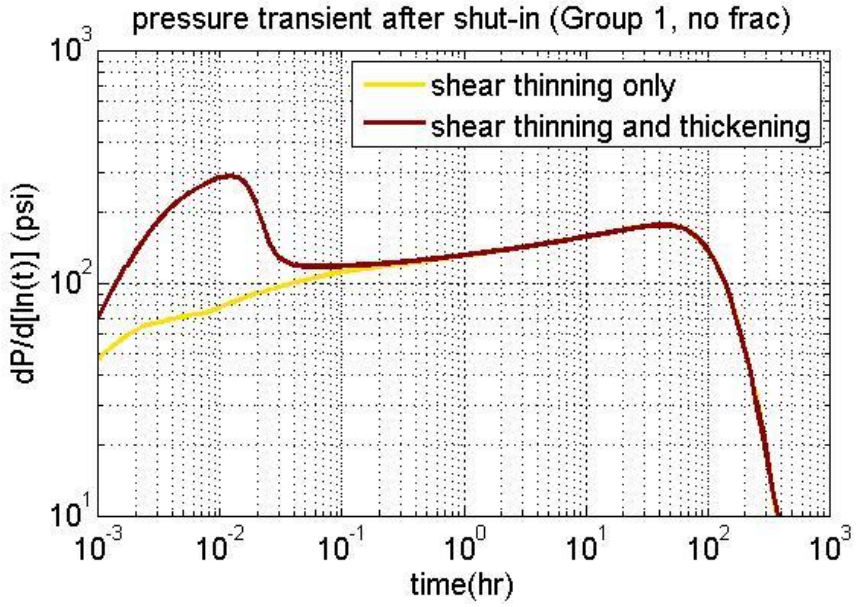

Figure 5-11 shut-in pressure transients of the non-Newtonian fluid for the regular pore pressure cases (Group 1, no frac)

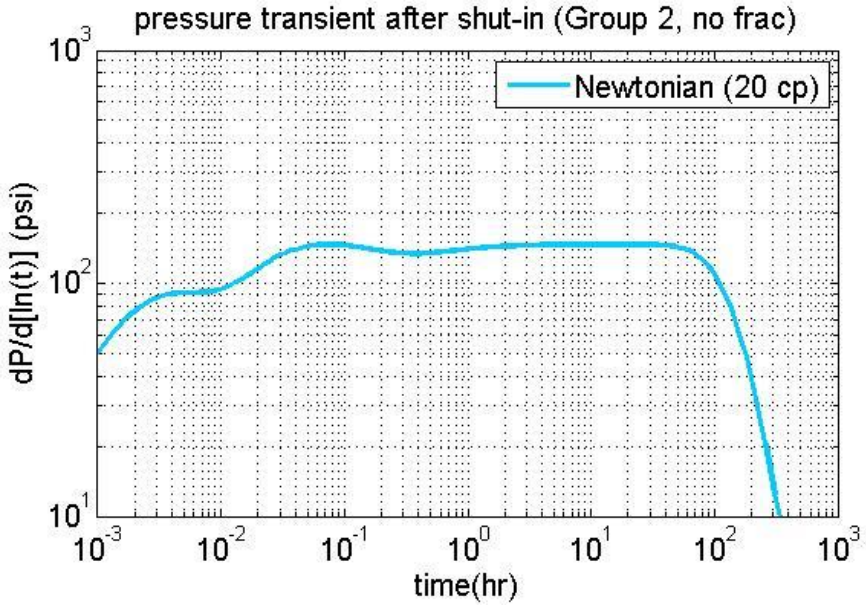

Figure 5-12 shut-in pressure transients of the Newtonian fluid for the overpressured cases (Group 2, no frac)

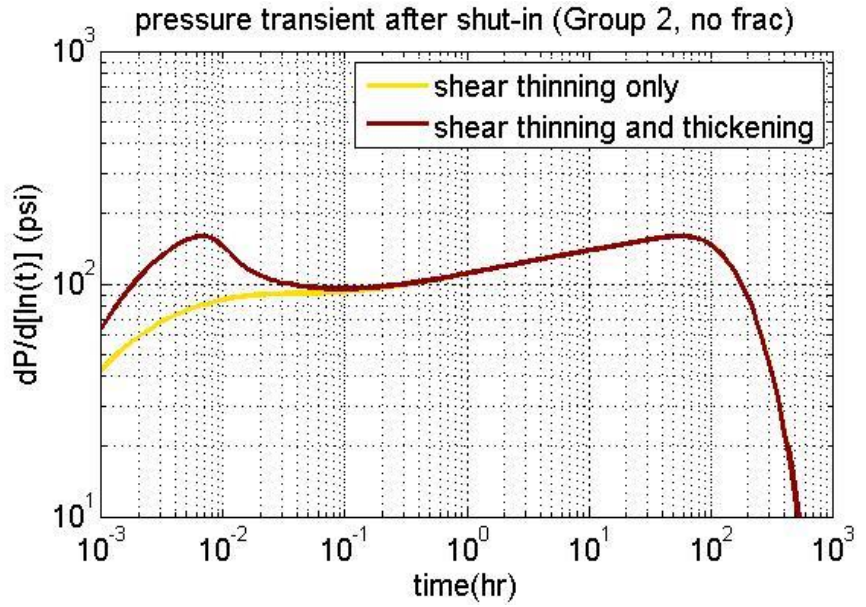

Figure 5-13 shut-in pressure transients of the non-Newtonian fluid for the overpressured cases (Group 2, no frac)

5.3.2 Well shut-in with long induced hydraulic fractures

In this group of simulations, a hydraulic fracture was permitted to form. The remote horizontal stresses were set at low values to represent a relatively overpressured reservoir. The half-lengths of the fractures induced in the three simulations were 120 m, 150 m, and 150 m, for the Newtonian fluid, the shear thinning polymer fluid, and the polymer fluid with both shear thinning and thickening viscosity, respectively.

Figure 5-14 and Figure 5-15 show the shut-in pressure transients using the derivative plots. Similar to the results in the no fracture cases, the shut-in pressure transients of the polymer fluid with and without shear thickening viscosity are nearly identical, indicating the domination of shear thinning behavior after the shut-in. During the early shut-in periods, linear flow regimes can be diagnosed for all the three cases discussed, with a slope of 0.43, 0.41 and 0.41 on the log-log scales, respectively. There are points with discontinuities on the derivative curves representing the fracture closures at 5.5 hrs, 8.9 hrs, and 8.9 hrs, respectively.

To verify the identifications of fracture closure, diagnostic curves were plotted as shown in Figure 5-16. This figure shows pressure as a function of the square root of the time. The linear flow regime is expected right after the well shut-in, before fracture closure. Therefore, the point in time when the curve deviates from a straight line should be the end of the linear flow regime and thus, the onset of fracture closure. The times read from Figure 5-14 and Figure 5-15 are consistent with those from Figure 5-16.

Finally, movies of fracture aperture versus time were made to directly observe when closure occurred. Snapshots in time are demonstrated in Figure 5-17. The residual aperture is a value set in CFRAC that represents the fracture aperture at the moment of closure. In these simulations, the residual aperture was set 0.5 mm. At the point when the fracture aperture reaches the residual aperture everywhere along the fracture, the fracture

has mechanically closed. The figures indicate closure times consistent with the interpretations from the three previous figures.

To summarize, the simulations indicate that the presence of a long hydraulic fracture can be diagnosed from the pressure transient after shut-in. The diagnosis strategy is barely affected by the fluid rheology. After a well is shut-in, shear thickening will affect the transient only at very early time. Subsequently, shear thinning behavior will be dominant, and the pressure transients of the polymer fluid with and without the shear thickening effect will be nearly identical.

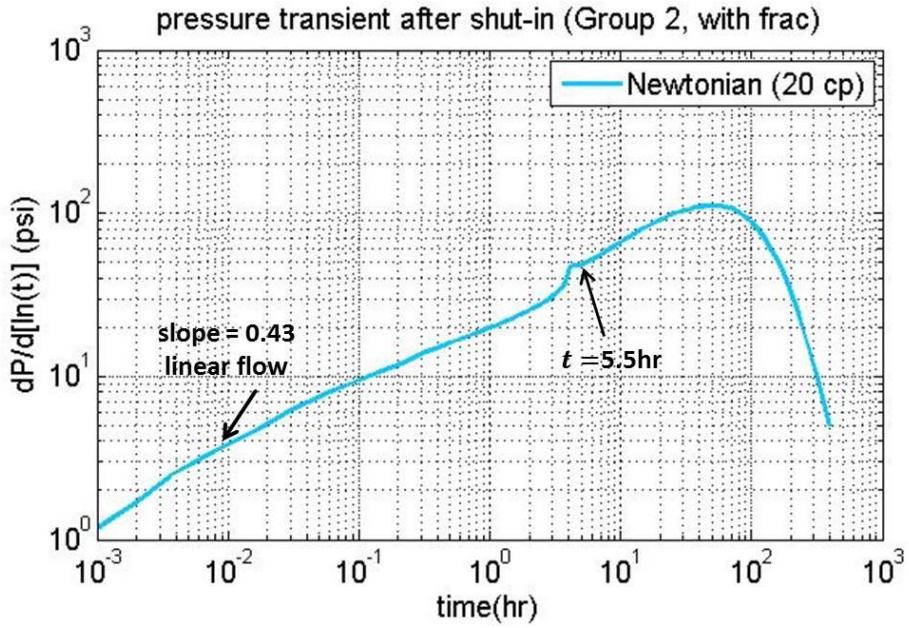

Figure 5-14 shut-in pressure transients of the Newtonian fluid for the overpressured cases (Group 2, with frac)

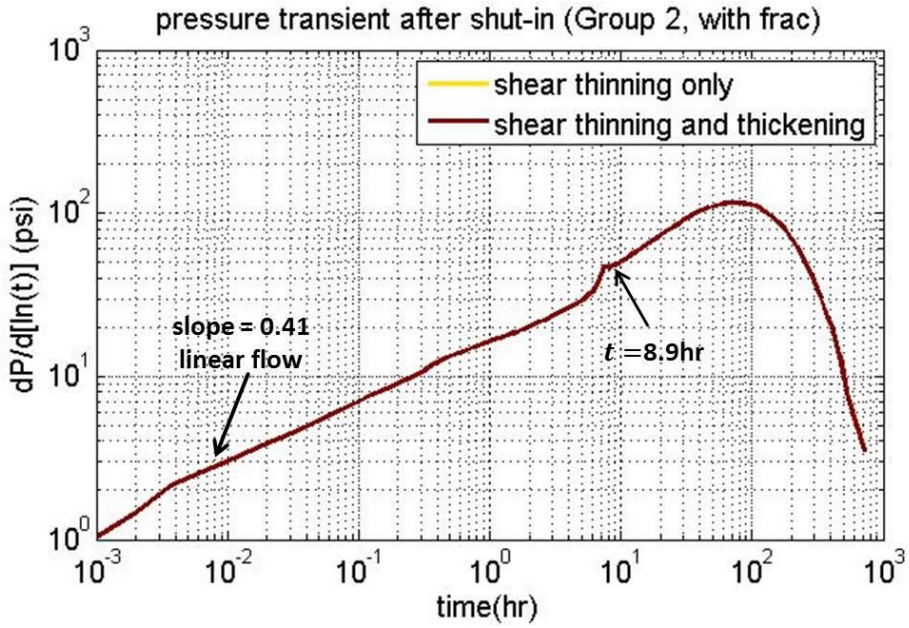

Figure 5-15 shut-in pressure transients of the non-Newtonian fluid for the overpressured cases (Group 2, with frac)

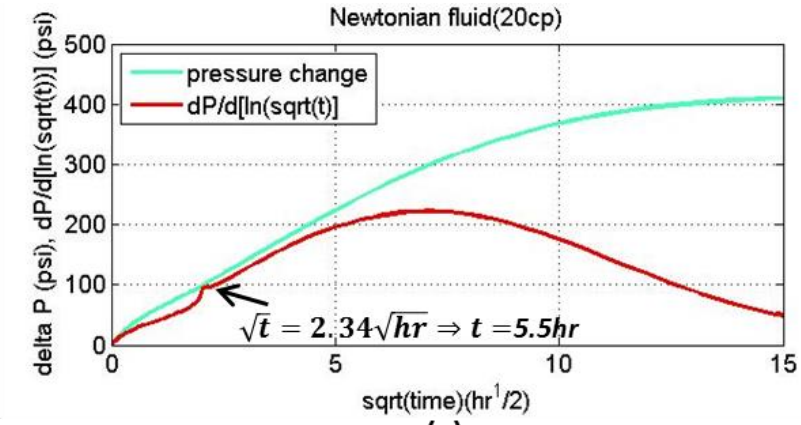

(a)

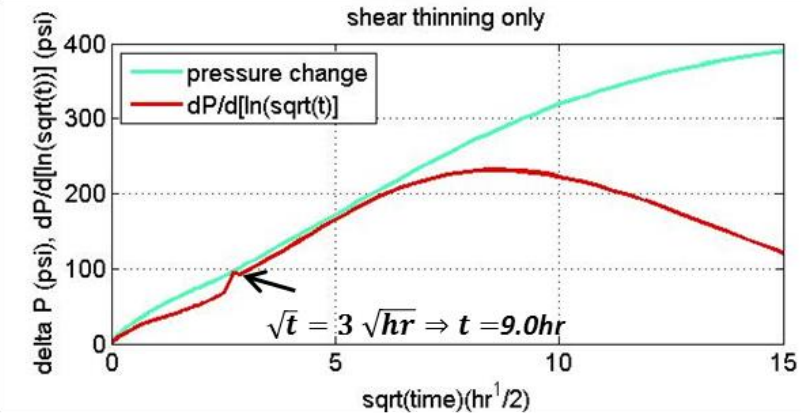

(b)

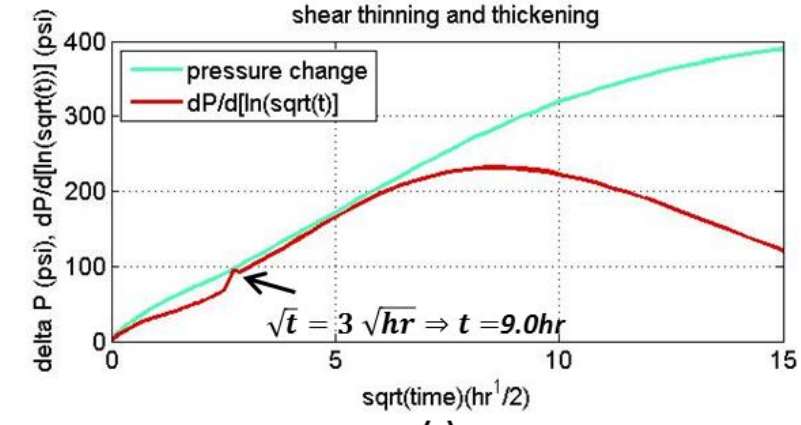

(c)

Figure 5-16 fracture closure diagnosis for the overpressured cases (Group 2): (a) Newtonian fluid; (b) shear thinning only; (c) with shear thickening.

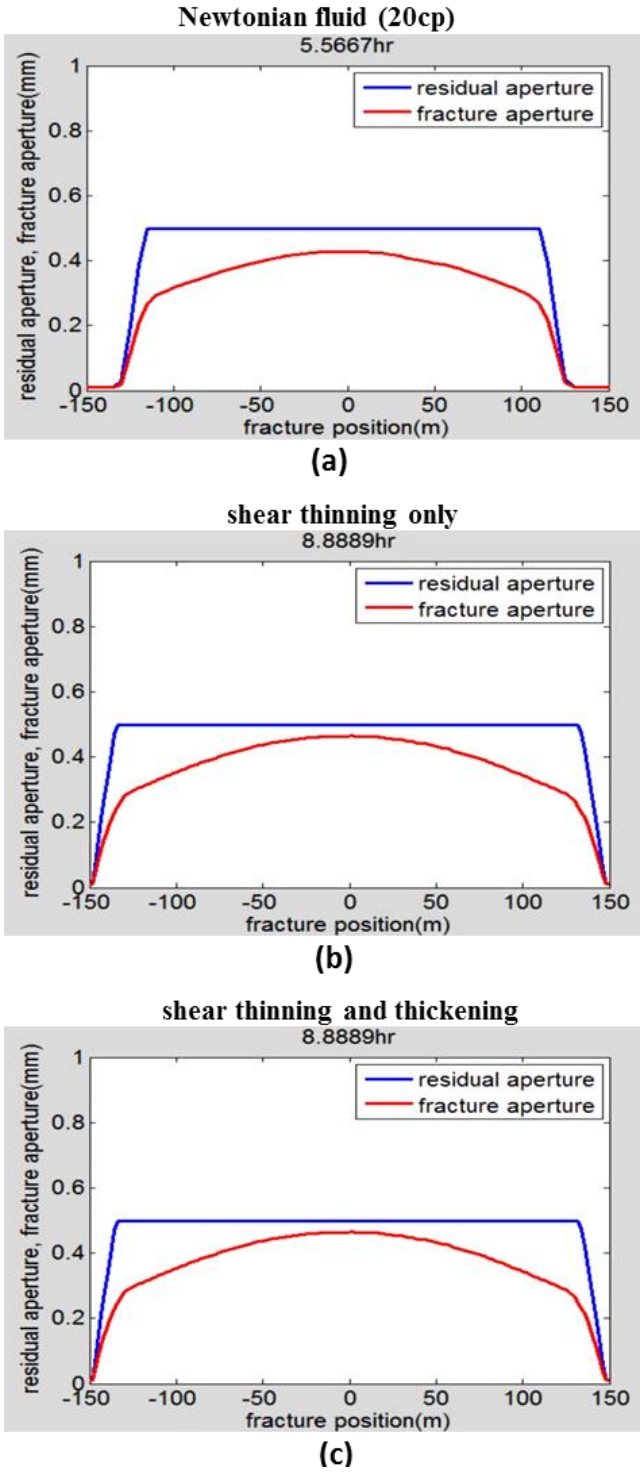

Figure 5-17 the fracture aperture at the closure for the overpressured cases (Group 2): (a) Newtonian fluid; (b) shear thinning only; (c) with shear thickening.

5.2.3 Well shut-in with short induced hydraulic fractures

In the regular reservoir pressure cases, the half lengths of the fractures induced by the three different fluids were 15m, 10m, and 10m, for the Newtonian fluid, the shear thinning polymer fluid, and the polymer fluid with both shear thinning and thickening viscosity, respectively. Because the reservoir pressure was significantly lower than the minimum principal stress, leakoff from the fractures was much more significant, causing shorter fractures.

Figure 5-18 and Figure 5-19 show the pressure transient results in the derivative plots. The cases with and without shear thickening showed very similar results, as in the previous cases. On the log-log derivative plots, linear flow was identified with a slope of 0.62, 0.63, and 0.63 before the fracture closure, and 0.46, 0.43 and 0.43 after the fracture closures for all the three fluids, respectively. It can be noted that due to the residual fracture aperture, linear flow occurred for some period of time after closure. Closure was apparent in Figure 5-18 ~ Figure 5-20 at very early time right after shut-in. Closure was indicated by the discotinuity of the derivative, rather than the end of linear flow, which was a bit later than mechanical closure.

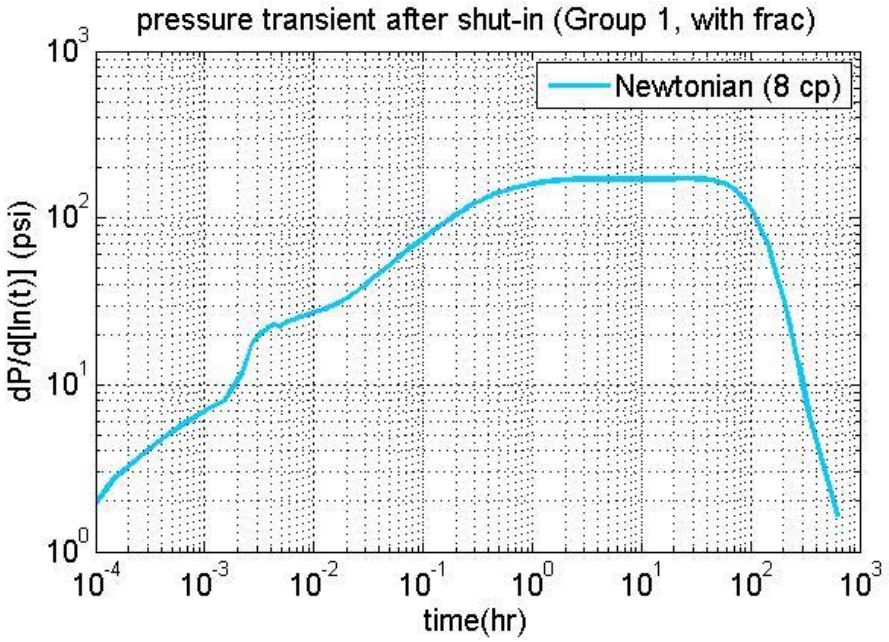

Figure 5-18 shut-in pressure transients of the Newtonian fluid for the normal pore pressure cases (Group 1, with frac)

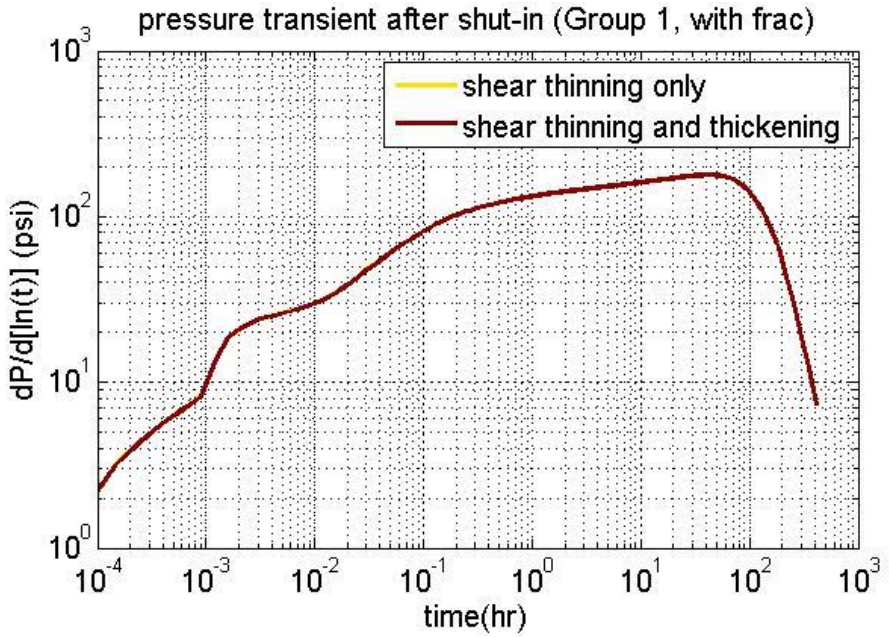

Figure 5-19 shut-in pressure transients of the non-Newtonian fluid for the normal pore pressure cases (Group 1, with frac)

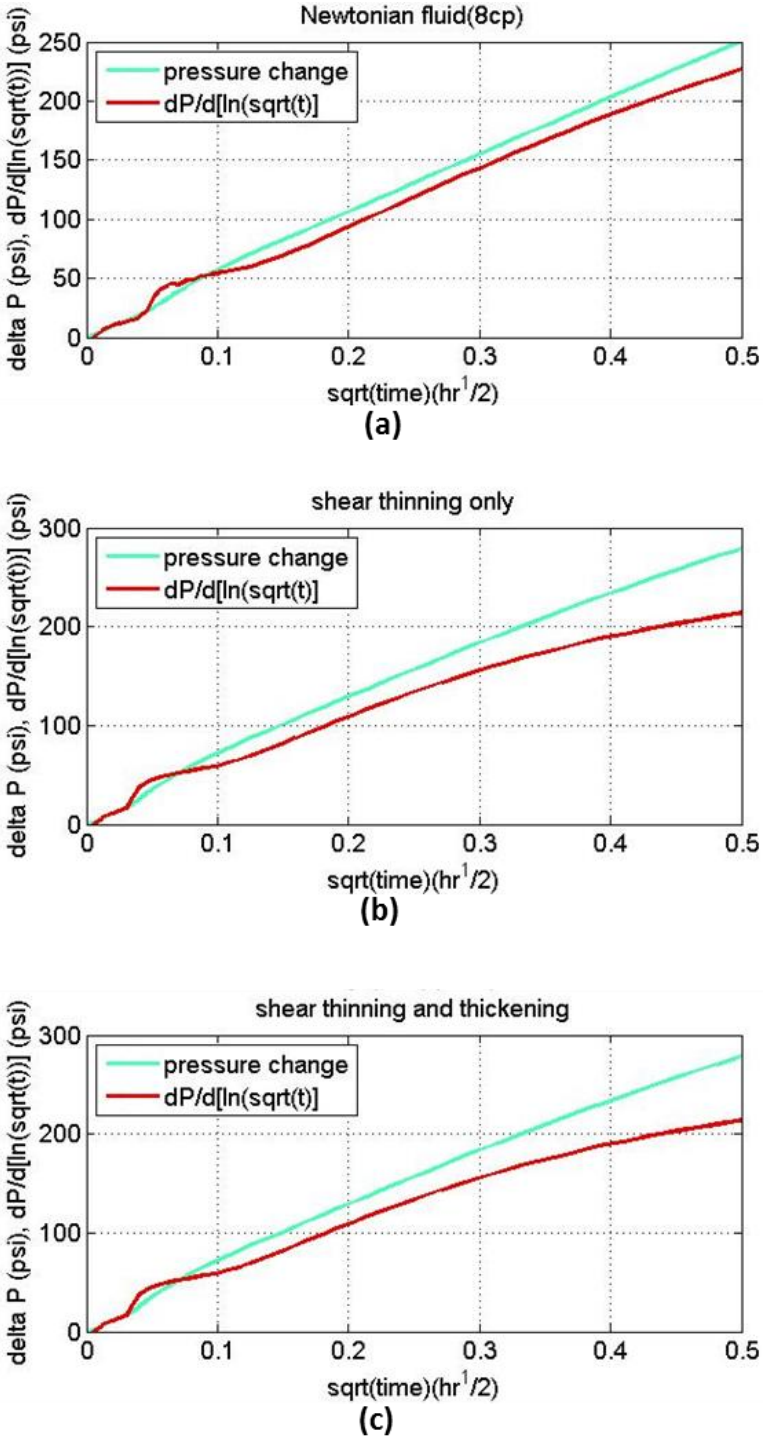

Figure 5-20 fracture closure diagnosis for the normal pore pressure cases (Group 1): (a) Newtonian fluid; (b) shear thinning only; (c) with shear thickening.

Chapter 6: Conclusions

- Shear thickening decreases polymer solution injectivity due to the high viscosity near the wellbore. This can cause or accelerate the formation of a hydraulic fracture.
- Induced hydraulic fractures substantially enhance polymer solution injectivity. If a hydraulic fracture forms, polymer injectivity with shear thinning and shear thickening will be nearly the same as the injectivity from a polymer with only shear thinning. Thus, the fracture causes the shear thickening to have a negligible effect on injectivity.
- Pressure transient analysis can be applied to diagnose the presence of a hydraulic fracture. These diagnostic methods were only modestly affected complex fluid rheology. Fracture closure was more difficult to identify in cases where the induced fracture was quite short.

REFERENCES

Ayirala, Subhash, Ernesto Uehara-Nagamine, Andreas Matzakos *et al.,*. 2010. A designer water process for offshore low salinity and polymer flooding applications. Proc., SPE Improved Oil Recovery Symposium, 24-28.

Bird, Byron R, Warren E Steward, Edwin N Lightfoot. 1960. *Transport phenomena* (Reprint).

Bird, Robert Byron, Robert Calvin Armstrong, Ole Hassager *et al.,*. 1977. *Dynamics of polymeric liquids*, Vol. 1, Wiley New York (Reprint).

Cannella, WJ, C Huh, RS Seright. 1988. Prediction of xanthan rheology in porous media. Proc., SPE Annual Technical Conference and Exhibition.

Carreau, Pierre J. 1972. Rheological equations from molecular network theories. *Transactions of The Society of Rheology (1957-1977)* **16** (1): 99-127.

Chang, Harry L. 1978. Polymer flooding technology yesterday, today, and tomorrow. *Journal of Petroleum Technology*.

Crawford, Paul B, RE Collins. 1954. Estimated effect of vertical fractures on secondary recovery. *Journal of Petroleum Technology* **6** (08): 41-45.

Delshad, M, GA Pope, K Sepehrnoori. 2000. UTCHEM version 9.0 technical documentation. *Center for Petroleum and Geosystems Engineering, The University of Texas at Austin, Austin, Texas* **78751**.

Delshad, Mojdeh, Do Kim, Oluwaseun Magbagbeola *et al.,*. 2008. Mechanistic interpretation and utilization of viscoelastic behavior of polymer solutions for improved polymer-flood efficiency. Proc., SPE/DOE Symposium on Improved Oil Recovery.

Denney, Dennis. 2013. Polymer Flooding in a Large Field in South Oman - Results and Plans. *Journal of Petroleum Technology*.

Dyes, A. B., C. E. Kemp, B. H. Caudle. 1958. *Effect of Fractures on Sweep-out Pattern*, Society of Petroleum Engineers (Reprint).

Fletcher, Alistair J. P., Stuart Weston, Andrew Kenneth Haynes *et al.,*. 2013. The Successful Implementation of a Novel Polymer EOR Pilot in the Low Permeability Windalia Field. Proc., SPE Enhanced Oil Recovery Conference, Kuala Lumpur, Malaysia.

Greaves, B. L., R. N. Marshall, J. H. Thompson. 1984. Hitts Lake Unit Polymer Project. Proc., SPE Annual Technical Conference and Exhibition, Houston.

Hirasaki, GH, GA Pope. 1972. Analysis of factors influencing the mobility and adsorption in the flow of polymer solution through porous media. *Society of Petroleum Engineers Journal*: 337-346.

Huh, Chun, Gary Arnold Pope. 2008. Residual oil saturation from polymer floods: laboratory measurements and theoretical interpretation. Proc., SPE Symposium on Improved Oil Recovery.

Lake, Larry W. 2010. *Enhanced Oil Recovery*. Richardson (Reprint).

Lee, Kyung Haeng. 2012. Impact of fracture creation and growth on well injectivity and reservoir sweep during waterflooding and chemical EOR processes. Proc., SPE Annual Technical Conference and Exhibition, Denver, Colorado, USA.

McClure, Mark. W. 2012. Modeling and characterization of hydraulic stimulation and induced seismicity in geothermal and shale gas reservoirs. PhD Thesis, Stanford University, Stanford, California.

Masuda, Yoshihiro, Ke-Chin Tang, Masashi Miyazawa *et al.,*. 1992. 1D simulation of polymer flooding including the viscoelastic effect of polymer solution. *SPE reservoir engineering* **7** (02): 247-252.

Moe Soe Let, Kathleen Priscilla, Renuka Natalie Manichand, Randall Scott Seright. 2012. Polymer Flooding a ~500-cp Oil. Proc., SPE Improved Oil Recovery Symposium, Tulsa, Oklahoma, USA.

Needham, Riley B, Peter H Doe. 1987. Polymer flooding review. *Journal of Petroleum Technology* **39** (12): 1,503-1,507.

Putz, A. G., J. M. Lecourtier, L. Bruckert. 1988. Interpretation of High Recovery Obtained in a New Polymer Flood in the Chateaurenard Field. Proc., SPE Annual Technical Conference and Exhibition, Houston.

Pye, David J, WB Gogarthy. 1964. Improved secondary recovery by control of water mobility. *Journal of Petroleum Technology* **16** (8).

Sandiford, BB. 1964. Laboratory and field studies of water floods using polymer solutions to increase oil recoveries. *Journal of Petroleum Technology* **16** (08): 917-922.

Seright, Randall S, J Mac Seheult, Todd Talashek. 2009. Injectivity characteristics of EOR polymers. *SPE Reservoir Evaluation & Engineering* **12** (05): 783-792.

Seright, RS. 1983. The Effects of Mechanical Degradation and Viscoelastic Behavior on Polyacrylamide Solutions. *Society of Petroleum Engineers Journal* **23** (03): 475-485.

Sheng, James. 2010. *Modern chemical enhanced oil recovery: theory and practice*, Gulf Professional Publishing (Reprint).

Sheng, James J, Bernd Leonhardt, Nasser Azri. 2015. Status of Polymer-Flooding Technology. *Journal of Canadian Petroleum Technology* (Preprint).

Smith, Frank W. 1970. Behavior of partially hydrolyzed polyacrlamide solutions in porous media. *Journal of Petroleum Technology* **22**.

Standnes, Dag Chun, Ingun Skjevrak. 2014. Literature review of implemented polymer field projects. *Journal of Petroleum Science and Engineering* **122**: 761-775.

Takaqi, Sunao, GA Pope, Kamy Sepehrnoori *et al.,*. 1992. Simulation of a successful polymer flood in the Chateaurenard field. Proc., SPE Annual Technical Conference and Exhibition.

Treiber, L. E., S. H. Yang. 1986. The Nature of Polymer Plugging and a Wellbore Treatment To Minimize It. Proc., SPE Enhanced Oil Recovery Symposium, Tulsa, Oklahoma, USA.

Valkó, Peter, Michael J Economides. 1995. *Hydraulic fracture mechanics*, Wiley New York, NY (Reprint).

Wang, Demin, Huifen Xia, Zhongchun Liu *et al.,*. 2001. Study of the mechanism of polymer solution with visco-elastic behavior increasing microscopic oil displacement efficiency and the forming of steady" Oil thread" flow channels. Proc., SPE Asia Pacific Oil and Gas Conference and Exhibition.

Wang, Dongmei, Peihui Han, Zhenbo Shao *et al.,*. 2008. Sweep-improvement options for the Daqing oil field. *SPE Reservoir Evaluation & Engineering* **11** (01): 18-26.

Yerramilli, Sanjay Surya, Pacelli Zitha, Ramesh Chandra Yerramilli. 2013. Novel Insight into Polymer Injectivity for Polymer Flooding. Proc., 10th SPE International Conference and Exhibition on European Formation Damage, Noordwijk, The Netherlands.

Zechner, Markus, Torsten Clemens, Thomas Gumpenberger *et al.,*. 2013. Flow of Polyacrylamide Polymers in the Near-Wellbore-Region, Rheological Behavior within Induced Fractures and Near-Wellbore-Area. Proc., SPE Annual Technical Conference and Exhibition, New Orleans, Louisiana, USA.